Design optimization of an electron-to-photon conversion target for ultra-high dose rate x-ray (FLASH) experiments at TRIUMF

Nolan Esplen, Luca Egoriti, Bill Paley, Thomas Planche, Cornelia Hoehr, Alexander Gottberg, and Magdalena Bazalova-Carter

2022

IOP Publishing Phys. Med. Biol. 67 (2022) 105003 https://doi.org/10.1088/1361-6560/ac5ed6

Physics in Medicine & Biology

IPEM Institute of Physics and Engineering in Medicine

OPEN ACCESS

RECEIVED
13 October 2021

REVISED
23 February 2022

ACCEPTED FOR PUBLICATION
17 March 2022

PUBLISHED
12 May 2022

PAPER

Design optimization of an electron-to-photon conversion target for ultra-high dose rate x-ray (FLASH) experiments at TRIUMF

Nolan Esplen[1], **Luca Egoriti**[2,3], **Bill Paley**[3], **Thomas Planche**[3], **Cornelia Hoehr**[1,3], **Alexander Gottberg**[1,3] **and Magdalena Bazalova-Carter**[1]

[1] Department of Physics and Astronomy, University of Victoria, Victoria, BC, Canada
[2] Department of Chemistry, University of British Columbia, Vancouver, BC, Canada
[3] TRIUMF, Vancouver, BC, Canada

E-mail: nolane@uvic.ca

Keywords: FLASH, radiotherapy, ultrahigh dose-rate, megavoltage x-ray, target design, Monte Carlo, thermomechanical

Supplementary material for this article is available online

Abstract

Objective. To develop a bremsstrahlung target and megavoltage (MV) x-ray irradiation platform for ultrahigh dose-rate (UHDR) irradiation of small-animals on the Advanced Rare Isotope Laboratory (ARIEL) electron linac (e-linac) at TRIUMF. Approach. An electron-to-photon converter design for UHDR radiotherapy (RT) was centered around optimization of a tantalum–aluminum (Ta–Al) explosion-bonded target. Energy deposition within a homogeneous water-phantom and the target itself were evaluated using EGSnrc and FLUKA MC codes, respectively, for various target thicknesses (0.5–1.5 mm), beam energies ($E_{e-} = 8$, 10 MeV) and electron (Gaussian) beam sizes ($2\sigma = 2$–10 mm). Depth dose-rates in a 3D-printed mouse phantom were also calculated to infer the compatibility of the 10 MV dose distributions for FLASH-RT in small-animal models. Coupled thermo-mechanical FEA simulations in ANSYS were subsequently used to inform the stress–strain conditions and fatigue life of the target assembly. Main results. Dose-rates of up to 128 Gy s^{-1} at the phantom surface, or 85 Gy s^{-1} at 1 cm depth, were obtained for a 1 $\times$ 1 cm^2 field size, 1 mm thick Ta target and 7.5 cm source-to-surface distance using the FLASH-mode beam ($E_{e-} = 10$ MeV, $2\sigma = 5$ mm, $P = 1$ kW); furthermore, removal of the collimation assembly and using a shorter (3.5 cm) SSD afforded dose-rates >600 Gy s^{-1}, albeit at the expense of field conformality. Target temperatures were maintained below the tantalum, aluminum and cooling-water thresholds of 2000 °C, 300 °C and 100 °C, respectively, while the aluminum strain behavior remained everywhere elastic and helped ensure the converter survives its prescribed 5 yr operational lifetime. Significance. Effective design iteration, target cooling and failure mitigation have culminated in a robust target compatible with intensive transient (FLASH) and steady-state (diagnostic) applications. The ARIEL UHDR photon source will facilitate FLASH-RT experiments concerned with sub-second, pulsed or continuous beam irradiations at dose rates in excess of 40 Gy s^{-1}.

1. Introduction

In the current scope of radiotherapy research and development there has been a recent revival of interest in ultra-high dose rate irradiation as a potential means of widening the therapeutic window. This attention is owed in no small part to the promising normal tissue sparing effects that have been repeatedly demonstrated through high-dose, sub-second treatment fractions at dose rates typically exceeding 100 Gy s^{-1} which has been broadly dubbed the 'FLASH' effect (Favaudon *et al* 2014, Montay-Gruel *et al* 2017, Bourhis *et al* 2019, Vozenin *et al* 2019). As a result, the demand for new radiation sources capable of achieving the requisite dose rates has grown substantially and yet relatively few compatible sources exist today. Increasing accessibility to a variety of radiation sources and enabling technologies therefore remains important to facilitate ongoing research aimed at

improving our understanding, and thus safe exploitation, of FLASH radiotherapy (FLASH-RT) in pre-clinical trials and beyond.

To date, FLASH-RT literature has been dominated by low-energy electron accelerators (Loo *et al* 2017, Jaccard *et al* 2018, Vozenin *et al* 2018, Jorge *et al* 2019, Lempart *et al* 2019, Simmons *et al* 2019) and, more recently, proton accelerators (Beyreuther *et al* 2019, Buonanno *et al* 2019, Girdhani *et al* 2019, Darafsheh *et al* 2020, Kim *et al* 2021). Photon modalities, on the other hand, have seen comparatively limited adoption due to the relative unavailability of ultra-high dose rate (UHDR) x-ray sources capable of achieving clinically-relevant megavoltage (MV) beam energies (Esplen *et al* 2020, Gao *et al* 2020). Moreover, while FLASH-RT has been successfully delivered using synchrotron-generated kilovoltage (kV) x-rays (Montay-Gruel *et al* 2018), the limited scalability and accessibility of such sources, low penetration of kV photons and the need to use scanned micro/mini-beams in forming UHDR broad beams, serve as limiters to wider adoption. MV x-rays therefore remain as an attractive modality for a future clinical translation of FLASH-RT owing to their highly penetrating nature and, thus, ability to treat tumors at greater depths in tissue. Established accelerator technologies, intensity modulation techniques and treatment planning software also exist which are specific to high energy x-rays and could be adapted for FLASH assuming multi-directional beam delivery can be implemented. By contrast, the prevailing particle FLASH modalities must overcome major barriers ahead of clinical translation. Electron FLASH, for example, may require the use of compact very-high energy electron (VHEE) accelerators (i.e. high gradient or laser acceleration) to enable treatment at greater depths; such sources exist, but require further development to keep pace with the competing modalities in terms of routine application and reliability. Meanwhile, proton FLASH leverages relatively costly infrastructure, excepting those clinical facilities that may be retrofitted, and is subject to the dosimetric challenges associated with FLASH treatment planning using active scanning techniques (van Marlen *et al* 2020) or field-size dependent dose-rate limitations in passive scattering systems (Esplen *et al* 2020).

To facilitate FLASH-compatible x-ray beam generation, already existing high-power sources can be employed; for example, superconducting electron linear accelerators (e-linacs) may be used to deliver high-intensity MeV electron beams to purpose-built bremsstrahlung conversion targets in order to generate the requisite UHDR photon field, while simultaneously providing access to the highly flexible beam parameter space which is unique to the underlying electron source. The development of a photon conversion target suitable to this application represents a primary motivator for this work.

In general, one of the primary difficulties with high-power MV photon sources relates to the bremsstrahlung conversion of electrons to photons in high atomic number (Z) targets. Due to an inherently low conversion efficiency, however, high-Z bremsstrahlung targets designed for a FLASH-compatible UHDR x-ray source must be capable of withstanding very high (i.e. kW) instantaneous beam power, which produces correspondingly high thermal stresses and associated damage within the converter (Esplen and Egoriti 2020, Esplen *et al* 2020). Furthermore, the target thickness must be optimized for the beam energy, or energy range, of interest so as to maintain UHDR compatibility by minimizing excessive self-attenuation while maximizing cooling performance and ensuring structural integrity over many thermal cycles (i.e. beam pulses). These considerations ultimately motivate the use of thin, sub-centimetric targets for which thermal strain and fatigue become significant challenges during design optimization and a limiter to achievable beam power. Thin-target photon converters have been used in the context of target design for industrial and food processing irradiators and therefore helped form a basis for the design framework employed herein (Miller 2005).

In this work, the development of a static tantalum (Ta) conversion target and Aluminum (Al) flange using an explosion-bonded interface (Egoriti *et al* 2020) has been explored with the goal of optimizing dose-rates within the thermomechanical constraints of the target system. The Ta–Al converter, and ancillary systems, have been developed for use on the high-powered electron linac of the Advanced Rare Isotope Laboratory (ARIEL) at TRIUMF (Vancouver, CA). There, a 10 MeV beam dump is being retrofitted to accommodate the new target flange alongside a preclinical treatment apparatus, while preserving its functionality as a low-power dump for e-linac development. The overarching goal was to develop a UHDR platform that will enable time scales of irradiation and intra-pulse dose-rates which are compatible with the prevailing definition of FLASH (i.e. $t < 0.5$ s, UHDR > 40 Gy s^{-1}) (Bourhis *et al* 2019, Montay-Gruel *et al* 2021). Meanwhile, the driving ARIEL e-linac could allow for flexible variation of these temporal beam parameters, namely the pulse time structure and instantaneous (intra-pulse) dose-rates for a given average dose-rate and prescribed dose.

The primary objective of this study was to design and fabricate a modular, cost-effective, yet robust, static photon converter for a 1 kW FLASH beam. The UHDR x-ray target was designed by way of dose-rate and thermomechanical optimization using Monte Carlo (MC) and finite element analysis (FEA) simulation methods. In what follows, the design process and theoretical performance results of the final prototype will be presented.

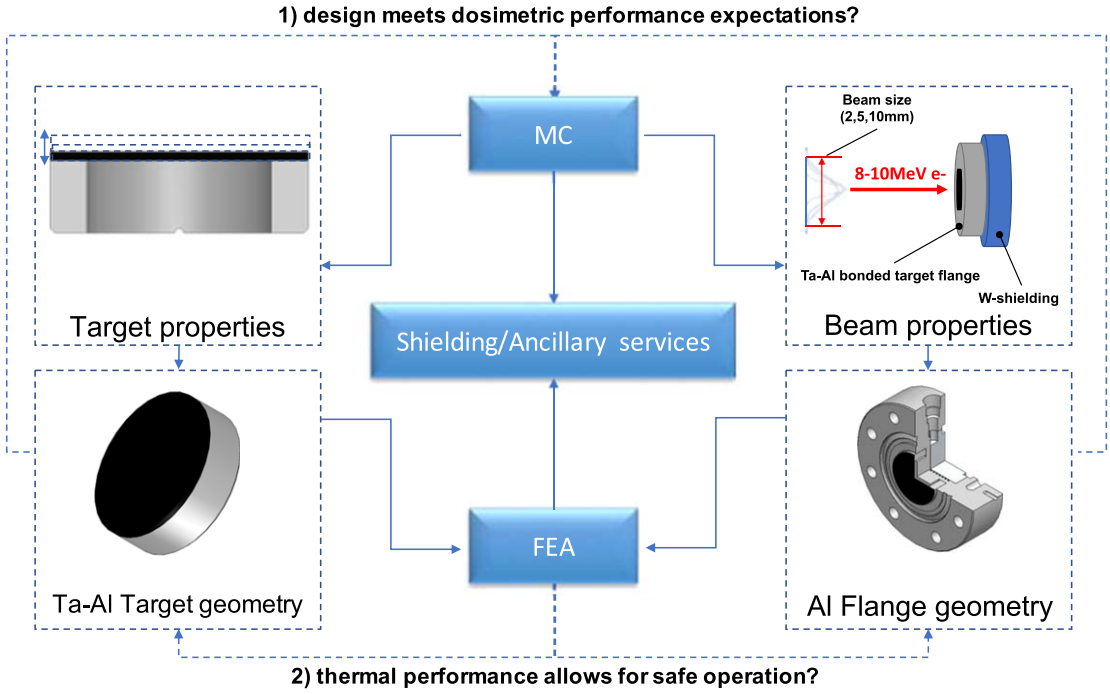

Figure 1. Schematic illustration of the ARIEL FLASH converter iterative design process, which included optimization with respect to target thickness, beam energy and size, thermal contacts, water cooling strategy and vacuum interfaces. Design limits were set through dosimetric (1) and thermal (2) performance goals that had to be simultaneously met.

Table 1. Summary of MC simulation parameters to be optimized in this work.

Power	1 kW
Energy	8, 10 MeV
Electron Beam Size	2, 5, 10 mm
Target Thickness	0.5, 1.0, 1.5 mm

2. Materials and methods

The development of the ARIEL UHDR x-ray source and FLASH irradiation platform has centered on the design and optimization of a target flange (converter). In addition, the converter is required operate as a non-UHDR beam dump for the ARIEL e-linac under normal (diagnostic mode) operation, which imposed constraints on the target design unique to its use-case at TRIUMF. Designing a suitable converter geometry was an iterative process (figure 1) in which MC simulations (section 2.1) informed geometric constraints while the detailed design and overall assembly were informed using thermomechanical simulations (section 2.2). A detailed overview of the aforementioned methods is presented in the following sections and a summary of the simulation parameter space is provided in table 1.

2.1. Monte Carlo simulations of x-ray beam production

2.1.1. Source description: The ARIEL e-linac at TRIUMF

The MC simulation of the bremsstrahlung target and resultant dose calculations were completed using a simplified model of the electron beam that will be delivered by the ARIEL superconducting e-linac at TRIUMF (Vancouver, BC).

The ARIEL e-linac is capable of delivering a high-powered megavoltage electron beam to experiments with excellent flexibility in the choice of physical beam parameters. The time-structure of the beam is nominally characterized by the injector frequency of 650 MHz that produces a continuous (CW) beam, to which a user-specified duty factor between 0.05% and 100% may be applied (Ames *et al* 2016). Specification of the duty factor allows for varying the average electron beam current over a wide range to enable both conventional and UHDR irradiations and, when paired with a low bunch charge (i.e. 0.15 pC), mitigates the need for retuning of e-linac parameters between modes.

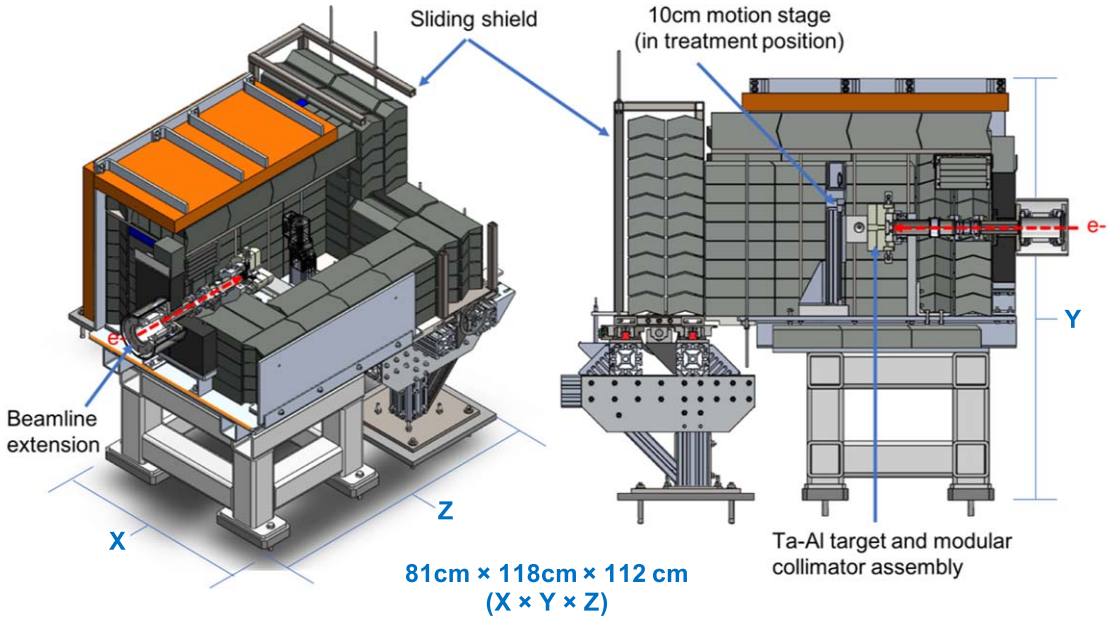

Figure 2. Computer-aided design (CAD) model of the ARIEL FLASH irradiation platform at TRIUMF. A retrofitted beam dump is leveraged to support a new, modular small-animal treatment apparatus which includes: Ta–Al target flange (which is also the vacuum window), modular x-ray collimator, electron collimator and target protection system, insulated beamline extension (for real-time current readback), sliding shield and access hatch, 10 cm vertical-motion treatment stage, and small-animal (i.e. mouse) localization/immobilization assembly.

At the location of the FLASH conversion target flange, an existing beam dump is being retrofitted for FLASH radio-biological experiments (figure 2). Here, an electron beam can be delivered at energies between 300 keV and 10 MeV, using an average beam power of up to 1 kW, and the emitted x-ray field propagates through the vacuum flange to the ambient air immediately downstream. Operation in a CW diagnostic mode shall be preserved for beam development at a maximum average beam power of 200 W.

For the purposes of MC simulation, the time-structure of the beam was considered to be continuous by neglecting any possible duty factor. For each simulated case, the electron beam was assumed to be perfectly monoenergetic with the beam spot size modeled as an axisymmetric 2D-Gaussian with a corresponding size characterized by the profile 2σ. At the location of the converter, a zero dispersion beam can theoretically be tuned while maintaining a nearly circular profile ($Y_{\mathrm{rms}} = X_{\mathrm{rms}}$) for $2\sigma \in [2,\ 10]$ mm (Shelbaya *et al* 2021) which motivates the aforementioned simplifying assumptions regarding the electron beam properties.

2.1.2. Target description: the electron-to-photon converter

The FLASH photon-converter flange presented here has been designed for routine, modular installation at the end of a horizontal beamline on the ARIEL e-linac, while considering the various space-limiting and safety constraints placed therein. The design included a tantalum thin-target 'window' (figure 3(a)) and aluminum body assembled by way of an interference (shrink) fit between an explosion bonded Ta–Al target insert (plug) and a water-cooled T6-tempered Al-6061 flange (figures 3(b), (c)). Aluminum was removed from the plug after explosion bonding, thereby creating the aluminum cylindrical interface (corona) attached to the tantalum layer.

One major requirement for converter design was to ensure that the primary electrons entering the flange would be stopped fully to avoid an excessive electron surface dose in the phantom. To achieve this, the combined thickness (t) of the tantalum target and aluminum flange body in the beam direction exceeded the CSDA range of the highest (10 MeV) energy electrons [i.e. at 10 MeV: $R_{\mathrm{CSDA,Ta}} = 0.3728$ cm; $R_{\mathrm{CSDA,Al}} = 2.1716$ cm]. Mathematically this condition can be described as follows (Miller 2005):

$$\left(\frac{t}{R_{CSDA}}\right)_{Ta} + \left(\frac{t}{R_{CSDA}}\right)_{Al} > 1.0. \tag{1}$$

It should be noted that, for all MC simulations presented herein, the aluminum flange thickness was fixed at 1.9 cm based on practical manufacturing considerations. For a nominal 1 mm tantalum target thickness, the left-side of equation (1) equates to 1.14, a value which exceeds unity and therefore satisfies the condition that the left-hand side exceeds unity. The implications of target thickness will be discussed in the context of the simulation results (section 3.1).

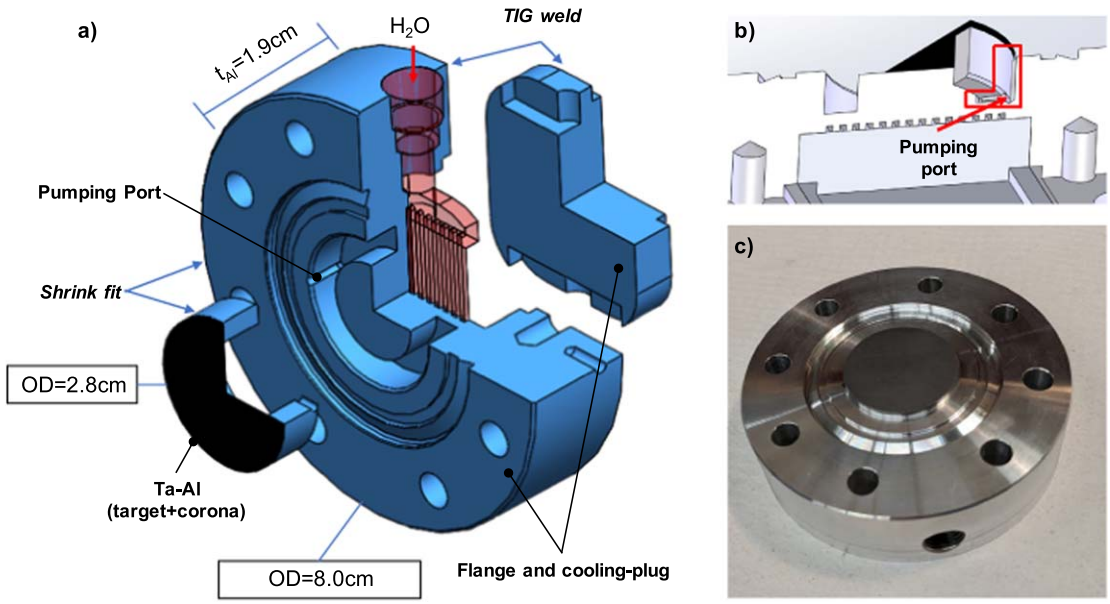

Figure 3. Sectioned and exploded CAD model for the conversion target (a) in which the various components and assembly methods (italicized) are outlined. Included are the tantalum target (black), aluminum corona and flange (blue) and cooling water channels (red). A close-up view of the target 'window' is shown (b) with the vacuum (conductance-limited) pumping port labelled. The assembled prototype is also pictured (c). [TIG = tungsten inert gas welding; OD = outer diameter; t_{Al} = flange thickness].

The selection of tantalum for the target was predicated on the need for a high-Z material that would maximize the bremsstrahlung x-ray conversion efficiency, while also providing favorable thermomechanical properties, most notably a high melting point and excellent ductility. The robustness of tantalum under high heat loads, good tolerance to radiation damage, and long lifetime under cyclic thermal loads supports the material as an effective choice for the thin-target design (LaForce *et al* 1971, Wilcox 2016). As compared to tungsten, which is commonly used in transmission x-ray targets, tantalum benefits our unique application by having a much lower ductile-to-brittle transition temperature that is important for maintaining ductility over the wide range of operational temperatures that it will be expected to withstand (Bechtold 1955, Farrell *et al* 1967, Davis 2001, Pan 2012). The use of aluminum 6061 in the flange, by contrast, is motivated by the comparatively low Z and photon interaction cross-section of the material, which also boasts high thermal and electrical conductivity to allow for improved heat transport.

The computer-aided design (CAD) models for the entire converter geometry (figure 3), alongside ancillary beamline components (figure 2), were designed in SolidWorks® Professional 2020 (Dassault Systemes, Vélizy-Villacoublay, France) and were directly imported into the subsequent thermal and mechanical finite element analysis (FEA) simulations (section 2.2). For the purposes of this work, the final prototype and associated simulation outputs will be presented.

2.1.3. Dose calculations and simulation geometry

MC dose calculations were employed to establish the theoretical performance of the converter based on identification of optimal target and beam parameters that ensure the performance goals of the project could be met within the thermomechanical constraints of the system. To this end, the converter flange assembly (figure 4) was modeled in EGSnrc/BEAMnrc (ver2020) (Rogers *et al* 2017).

To study the influence of target geometry and beam parameters on dose rate, a discrete set of parameters were investigated in the course of the target design optimization based on informed constraints. Specifically, the effect of target thickness ($t = 500$, 1000 and 1500 μm), electron beam size ($2\sigma = 2$, 5, 10 mm) and beam energy (E = 8, 10 MeV) were considered (table 1). The limited energy range was chosen for practicality with the converter design and suitability to MV UHDR irradiations. Note that beam size shall everywhere refer to the size of the primary electron beam, whereas field size refers uniquely to the x-ray beam and is defined by the downstream tungsten collimator. In all simulations, the x-ray fields were shaped by the 1×1 cm^2 collimator unless otherwise specified (i.e. for an open field).

In a first simulation step, the impinging electron beam was transported through the Ta–Al target and flange geometry. For each simulated configuration (table 1), 10^6 electrons with initial kinetic energies of either 8 or 10 MeV were made to impinge upon a thin tantalum film—the target 'window'—and transported through the water-cooled flange which comprised a 2 cm thick aluminum body (flange) and fifteen 1×1 mm^2 square

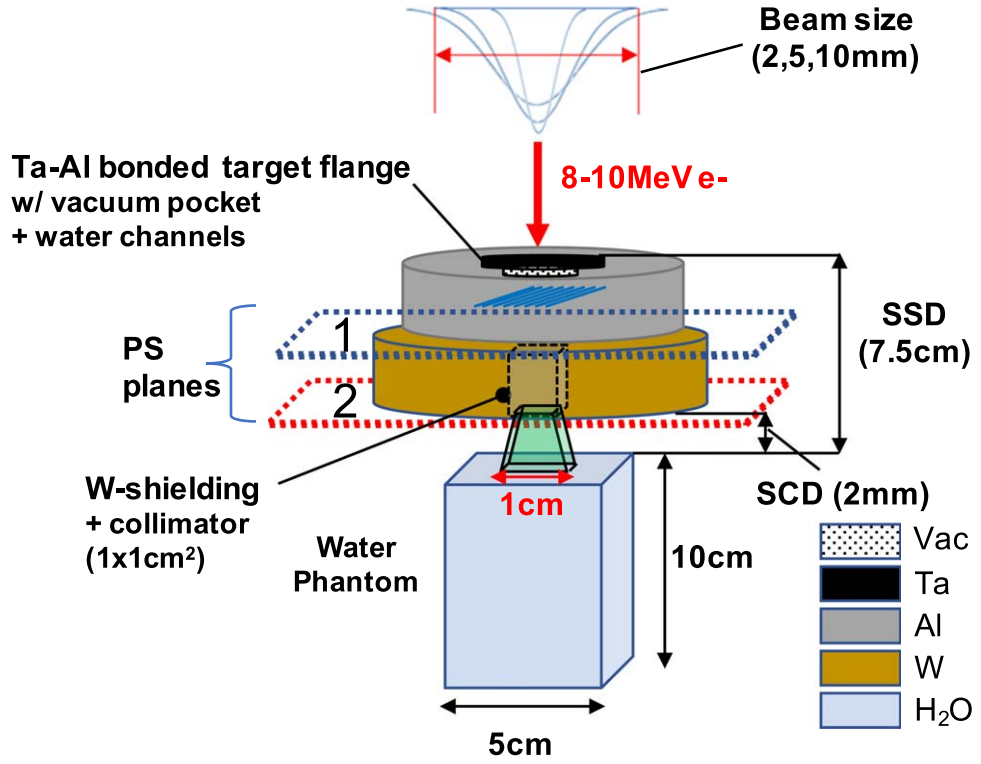

Figure 4. Schematic illustration of the water-cooled converter simulation geometry modeled in the EGSnrc MC codes. Phase-space (PS) scoring planes were located between the Al flange and W collimator, and at the 1×1 cm^2 collimator exit. The $5 \times 5 \times 10$ cm^3 phantom was located at a nominal distance of 7.5 cm for all DOSXYZnrc phantom simulations using files from PS#2 (red plane) as source inputs with the exception of the open field simulation, which used files from PS#1. The source-to-collimator distance (SCD) was fixed for all simulations at 2 mm, excepting the mouse phantom simulation (section 2.1.4) for which an SCD of 7 mm was used. A 1×1 cm^2 collimator was used to define the field size.

cross-sectional water channels. The 5 cm thick, 1×1 cm^2 field-size tungsten collimator was additionally included (figure 4) in order to produce a more representative treatment field size, and conformal dose distribution, along the beam central axis (CAX). Phase-space files were scored at various interfaces in order to facilitate the analysis of relevant beam properties (PS#1, 2; figure 4).

In order to improve the efficiency of the x-ray beam simulations, directional bremsstrahlung splitting with a splitting factor of 200 was used together with a bremsstrahlung cross-section enhancement factor of 20 in the tantalum target. To improve contaminant electron statistics, e−/e+ splitting was activated for the aluminum flange which was modelled using the FLATFILT geometry and included the cooling water channels and vacuum pocket.

In a second simulation step, the phase-space files generated in BEAMnrc were used as source inputs for depth-dose simulations in a $(5 \times 5 \times 10)$ cm^3 water phantom using the DOSXYZnrc code (Walters *et al* 2017). The phantom thickness was selected to ensure full backscatter conditions in a 10 MV beam rather than be representative of pre-clinical models. Each phase-space source contained $>10^7$ particles. The phantom was located at a source-to-surface distance (SSD) of 7.5 cm and the absorbed dose was scored in uniform 0.2 mm^3 voxels. The SSD was fixed at 7.5 cm, so as to represent the nearest location for the surface of small-animal models which will be placed in an irradiation jig (not shown) located immediately downstream of the collimator assembly. The air gap between the collimator exit surface and water phantom surface, or collimator-to-surface (CSD), was fixed at 2 mm unless otherwise specified.

For each DOSXYZnrc simulation, the full phase-space was run, without any recycling of particles, resulting in a statistical uncertainty within high-dose regions of less than 0.9%. The calculated dose, expressed in Gy/particle, was converted to dose-rate (Gy s^{-1}) by assuming the maximum beam current, for each beam energy, that would correspond to an average power of 1 kW (i.e. 0.1 mA for 10 MeV). The dose conversion was accomplished by way of the following formula: $\mathrm{d}D/\mathrm{d}t(\mathrm{Gy\,s^{-1}}) = \mathrm{d}D/\mathrm{d}t(\mathrm{Gy\,particle^{-1}}) \times I(\mathrm{A})/1.602\mathrm{e}^{-19}(\mathrm{C})$, where I is the time-invariant electron beam current in C s^{-1}. Unless otherwise specified, all PDD dose-rates are calculated as averaged values in a 0.5 cm^2 ROI about the CAX at each depth. Beam penumbra are calculated as the interpolated lateral distance between points on the beam dose profile which correspond to 80% and 20% of the maximum dose at a treatment depth of 1 cm.

For all EGSnrc simulations, the electron and photon kinetic energy cutoffs were set to 150 keV and 5 keV, respectively. Low energy physics, such as atomic relaxation, and Rayleigh scattering were included, while electron impact ionization was ignored. The xcom cross section data was used and all remaining EGSnrc input parameters were set to their default values. All simulations were run on 3.06 GHz 6-Core Intel® Xeon processors using a local high-performance computing cluster. The BEAM simulation time was between 39–50 h while each DOSXYZnrc simulation completed in <5 h.

2.1.4. In vivo *dose distribution using a rodent-morphic 3D-printed mouse phantom*

A brief MC study of the dose distribution in a sample mouse lung-irradiations was completed to demonstrate the theoretical dose distributions that might be expected for unidirectional, single-fraction irradiation of a mouse model *in vivo*. The material properties of the phantom are such that there is negligible energy-dependence for x-ray beam energies >1 MeV based on the effective atomic number and pre-dominance of the Compton scattering cross-section (Esplen *et al* 2019a, 2019b). However, for the purposes of this study, the materials in the lung and bone were selected to be that of a biological mouse as opposed to the polymeric materials comprising the 3D-printed phantom to be used for treatment dose verification ahead of planned irradiation campaigns. Specifically, ICRU Report 44 (ICRU 1989) densities were used for bone ($\rho = 1.6\,\mathrm{g\,cm^{-3}}$), lung ($\rho = 0.58\,\mathrm{g\,cm^{-3}}$) and soft tissue ($\rho = 1.06\,\mathrm{g\,cm^{-3}}$) body for the MC simulated mouse geometry.

For the purposes of this work, a single unidirectional lung irradiation was simulated in the mouse phantom using the reference 10 MV FLASH beam, generated in BEAMnrc (section 2.1.3) assuming a 5 mm electron beam size and a 1000 um thick tantalum target. The voxelized geometry data for the phantom was imported directly into DOSXYZnrc as an *.egsphant* file and the dose-rate for a 1 kW exposure was calculated for the $1 \times 1\,\mathrm{cm^2}$ collimated field (scored at PS2, figure 3) using the dose conversion specified in the previous section. A nominal treatment SSD of 8 cm (SCD = 7 mm, see figure 4) was used as it corresponded to the closest position for the irradiation and jig and motion stage assembly (figure 2). The beam was incident on the mouse right flank with beam isocenter assigned to the geometric center of the mouse lung. Dose contours were visualized using the online VICTORIA (Badun *et al* 2021) software while the dose-rate profiles are calculated for a central $0.5\,\mathrm{cm^2}$ ROI about the CAX from which lateral and depth-dose distributions could be derived.

2.1.5. Converter energy deposition and material activation

To provide accurate heat inputs to thermomechanical converter simulations (section 2.2) the FLUKA MC code (version 2020.0) was employed to score volumetric energy deposits throughout the flange and target geometries. These results were then used, with appropriate re-formatting, as power inputs to FEA simulations (section 2.2). FLUKA was employed in this capacity due to the existence of a well-developed pipeline that couples MC and downstream FEA simulations, along with flexible scoring options within the target geometry and calculations not available to EGSnrc, such as neutron transport and photo-activation.

For each electron beam size, 10^7 primary histories (8 or 10 MeV electrons) were transported through a model of the shielded irradiation platform (figure 2). The simulated converter geometry was as described in section 2.1.3, excepting the target thickness which was fixed at 1000 μm for the results presented herein. Three-dimensional energy deposition maps were scored in $0.5 \times 0.5 \times 1\,\mathrm{mm^3}$ voxels, and results were output in terms of power density ($\mathrm{W\,cm^{-3}}$) with statistical uncertainties of less than 2% for all voxels with power densities >1 $\mathrm{W\,cm^{-3}}$, including everywhere within the beam impingement region. Photo-fission and subsequent neutron activation within the entire irradiation station was simulated to evaluate the resultant activation and inform safe handling according to the possible equivalent dose to personnel. Equivalent dose was scored in $\mathrm{mSv\,hr^{-1}}$ at a distance of 0.5 m from the target center after 1 week of continuous CW irradiation at 1 kW and 10 MeV, equivalent to FLASH mode operation at 100% duty factor; this is opposed to the more realistic low-frequency scenario with <1 s beam-ON time and a low total number of irradiations (<50) lasting less than 1 week. Results assumed emission from a point source at the location of the target and without any self-attenuation in, or shielding of, the activated components for added conservatism.

For all FLUKA simulations, the transport energy threshold for delta rays (electrons) were set to 200 keV. Optional physics models that were implemented to include evaporation, coalescence, electro-magnetic dissociation (projectile and target), heavy-ion direct pair production. The standard cross-section libraries were used and no variance reduction was applied. Simulations were run on a quad-core i7–6700 CPU at 3.4 GHz and completed within 12 h.

2.2. FEA thermal and structural simulations of the electron-to-photon converter

Thermomechanical simulations were employed to establish an efficient and practical design for the compact photon converter flange. The FEA software package ANSYS® [2020 R2] (Canonsburg, PA) and, specifically, the static and transient Mechanical and Thermal modules in Workbench 2020 R2 were used to simulate the steady-

Table 2. Summary of custom FEA simulation and material parameters of relevance to thermal and structural (static and transient) modules. Quoted quantities are set to 50% of their calculated values, equivalent to applying a safety factor of 2.

Convective heat transfer coefficient (for water channels)	16 000 W m^{-2}
Thermal conductance (Al–Al, shrink fit)	2360 W m^{-2}
Thermal conductance (Ta–Al)	Ideal, bonded
Emissivity (Ta)	0.1
Interference fit (Al–Al, contact gap)	-1×10^{-5}
Strain-life model (Ta)	LaForce *et al* (1971)

state and transient thermomechanical responses. The parameterized design study considered the same configurations as for MC simulations (table 1). In addition, all FEA simulations utilized conservative assumptions as relates to physics inputs, including convection coefficients, water flow rates, and thermal conductance values by applying a safety factor of 2 in each case. In this way, an engineering safety margin could be built in while maintaining additional confidence in the robustness of the final design (table 2). Temperatures (°C), von Mises stress (Pa) and elastic/plastic strain (m/m) distributions were evaluated for each case. The von Mises stress applies to a yield criterion which states that where this stress is equal or greater than the yield strength of a material, defined under uniaxial tension, the material will yield. The von Mises yield criteria and subsequent stress–strain analyses were considered suitable to the ductile nature of the critical metallic target components.

SolidWorks® CAD geometries were imported into the ANSYS® design modeler while power density inputs, as calculated in FLUKA (section 2.1.3). An unstructured tetrahedral mesh, with element sizes of 0.7–1.5 mm, was used for the aluminum flange body while the Tantalum target plug was modeled using a hybrid hexahedral mesh, with element sizes of 0.1–0.5 mm, for improved regularity and accuracy; default mesher settings were otherwise employed. The resulting geometry comprised (3–7) $\times$ 10^5 elements. All interfaces (Ta–Al, and Al–Al) used in the downstream mechanical simulations were assumed to be bonded while the Al–Al shrink fit interface was assigned a manually-input thermal conductance of 4720 W m^{-2} K^{-1}, extrapolated from experimental data examining cylindrical Al interfaces under similar conditions (Barzelay *et al* 1955). In this case, the lowest temperature regime, modest (1000 psi) contact pressures, and a 65 microinch RMS surface roughness were assumed. The cooling channels were assigned a convective heat transfer coefficient (h) of 3.2 $\times$ 10^4 W m^{-2} K^{-1}, calculated based on the dittus Boelter correlation (Incropera and DeWitt 2002) for water in square cross-sectional channels with 1 mm hydraulic diameter; this value was verified using ANSYS computational fluid dynamic simulations (CFD module) which included the same water-cooling channel design as in the Mechanical simulations while assuming a water flow-rate of 4.5 lpm and bulk temperature of 30 °C. Thermal radiation effects for the target were included by setting a conservative emissivity of 0.1 on the tantalum surface. It is worth noting that both the heat transfer coefficient and Al–Al thermal conductance values used were input as 50% of their calculated values in order to elicit a safety factor of at least 2 (see table 2). In all structural simulations the engineering material data, including temperature-dependant ultimate tensile and yield strengths, linear expansion coefficients, density, elastic moduli, and conductivities, were taken from standard libraries or compiled reports on material properties such as for 6061-T6 aluminum (ASM International Handbook Committee 1991, Marquardt *et al* 2002) and tantalum (Schmidt and Ogden 1963, Ho *et al* 1974).

Fatigue analysis in the flange was approached separately for the tantalum and aluminum materials. The calculation of fatigue life in the tantalum layer followed from the assumption of a purely elastic stress–strain model and used the ANSYS fatigue tool's parameterized strain-life equations with Morrow mean-stress correction. The coefficients for the model were derived for the highest temperature data (1350 °F) in argon available from LaForce *et al* (1971). Tantalum plasticity was investigated in a set of simulations without fatigue modelling, but otherwise identical, where the stress and corresponding plastic strain within the entire flange geometry could be evaluated. For estimating the fatigue behavior of the aluminum parts, an empirical fit to ASME-derived stress-cycle curve data was used as the basis for estimating the fatigue life, or number of cycles (N), in the Al-6061 bodies (Yahr 1993, Schulz and Yahr 1995). The governing equation, which assumes fully reversed loading and thus requires the Goodman mean-stress corrected stress amplitude (S) as input, takes the following form:

$$S = \frac{14479}{\sqrt{N}} + 96.5 \text{ MPa}. \tag{2}$$

In the above formalism, S was calculated from the Goodman equation $S = S'/(1 - S_m/S_u)$, wherein S_m is the mean stress, or half the sum of the stress amplitude and shrink-fit pre-stress as calculated from the corresponding

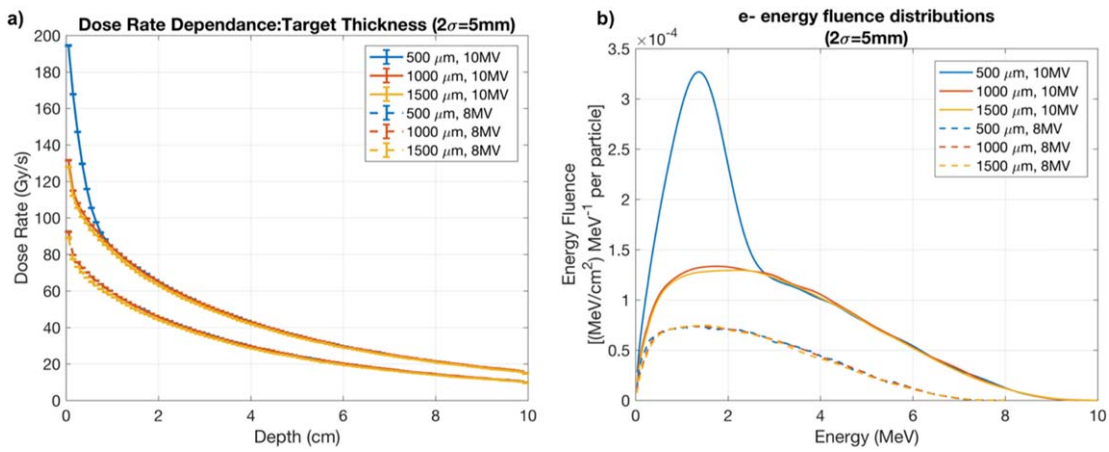

Figure 5. The effect of Ta target thickness on the dose-rates as a function of depth for both candidate beam energies (a) and a 1×1 cm^2 field size. A demonstration of the primary electron transmission in the 500 μm target configuration at 8 and 10 MeV is shown (b) by way of the electron energy fluence spectra which is normalized by the field size, energy bin width and number of primary histories.

ANSYS simulation, S_u is the ultimate tensile strength taken from the literature and S' is the stress amplitude for the case of non-fully reversed loading. Given that steady-state diagnostic operation at lower beam power accounts for the largest contributor to cyclic thermal loading, the aluminum corona is assumed to act as the fatigue-life limiting material, whereas for high-power FLASH (pulsed) operation, the fatigue life of the tantalum becomes relevant, particularly in off-normal condition use (i.e. accidental power spikes or beam trip). Radiation-induced embrittlement is not accounted for and oxidation is ignored due to the extremely low oxygen and hydrogen partial pressures in the UHV (10^{-9} mbar) beamline. However, it is recognized that pressures behind the target window may be elevated (up to 10^{-4} mbar) due to the reduced pumping speed afforded by the conductance-limited pumping port in the converter (figure 3) and may contribute a possible oxidation risk.

The time required for convergence during steady-state thermal simulations, which employed a single simulation step, was approximately 1 min, while transient thermal simulations utilized adaptive time stepping over 3 s of simulated time and converged within 30 min. Static structural simulations were completed using 10 substeps and converged in $<$30 min while transient simulations used the same time stepping parameters as the transient thermal analyses, converging within 6 h. All simulations were run in parallel (4 threads) on a quad-core i7–6700 CPU at 3.4 GHz.

3. Results

The results of MC simulations in a homogenous water phantom are presented in the forthcoming section (section 3.1). These results were used to motivate the selection of beam and target parameters for future irradiations and provided a basis for selecting the more conservative beam configurations for use in subsequent thermomechanical simulations (section 3.2). All MC results presented herein were simulated according to the methods outlined in section 2.1.

3.1. Monte Carlo simulation of x-ray beam production

The effects on depth-dose rates due to variation of the tantalum target thickness for both beam energies, keeping the electron beam size constant, is presented in figure 5. The 500 μm target showcases a large dose enhancement of up to 48% at shallow depths ($z < 1$ cm) for the 10 MV beam. This feature, absent in the 8 MV beam data, is contributed by an increase in low-energy primary electron transmission amounting to an 86.7% increase in electron energy fluence compared to the cases where only secondary electrons were present. This enhancement is illustrated via the electron energy fluence spectra for the 500 μm target at the surface of the water phantom for the 5 mm electron beam (figure 5(b)). The 1000 μm target, by contrast, proved capable of removing the primary electron fluence, leaving only secondary electrons generated within the flange body (Al) and W-collimator which are primarily responsible for the lack of a depth-dose build-up region.

The effects of changing electron beam size and energy were also considered for the 1000 μm tantalum target (figure 6). Figure 6(a) showcases the changes in dose-rate with an electron beam size across both candidate energies (8, 10 MeV). At 10 MV, a 6.8% depth-averaged increase in dose-rate is found by reducing the beam size from 10 mm to 5 mm; this difference is slightly reduced at 8 MV, with average difference of 6.0%. In contrast, there is only a marginal increase (1.4%) in dose-rate when further reducing beam size to 2 mm for both beam

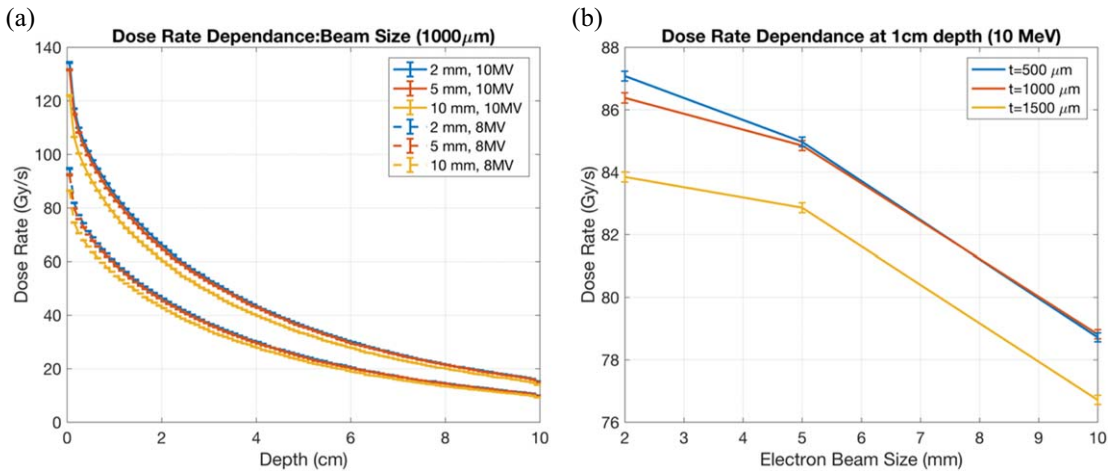

Figure 6. The effect of electron beam size (Gaussian 2σ) on the depth dose-rates for both candidate beam energies (a) on a 1 mm Ta target. A summary of the dose-rate dependence of the 1×1 cm^2 10 MV beam on target thickness and beam size, at a representative treatment depth of 1 cm in the water phantom, is presented in (b). The sample depth was selected for its relevance to pre-clinical treatments and to avoid the possibility of the dose-rate varying due to differences in the contaminant electron dose observed at the phantom surface.

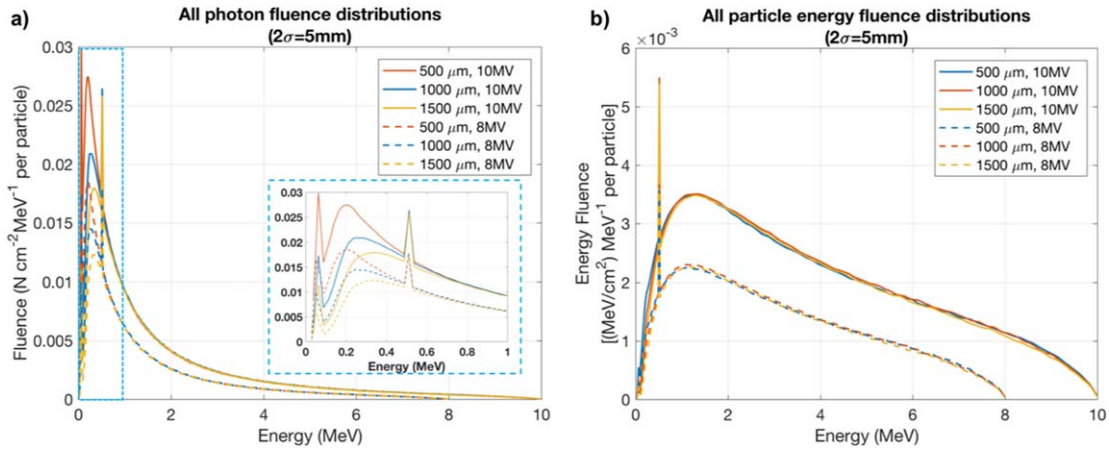

Figure 7. Normalized photon fluence (a) and total (all particle) energy fluence spectra (b) for beam configurations of interest in this work. The inset in (a) highlights the spectral range up to 1 MeV and illustrates the low-energy sensitivity of the electron beam spectra to changes in target thickness. All beams assumed the 5 mm (2σ) beam size. Spectral quantities are normalized by the field size, energy bin width and number of primary histories.

energies. Moreover, an incoming electron beam energy of 10 MeV yielded 31.7% higher dose-rates when compared to an 8 MeV beam, providing a clear incentive to employing the higher beam energy during FLASH irradiations.

A summary of the dose-rate dependence on electron beam size and target thickness are summarized by way of figure 6(b) for a 10 MV FLASH beam at the treatment SSD (7.5 cm) and depth ($z = 1$ cm) within the homogenous water phantom. The dose-rate plot in figure 6(b) shows low sensitivity to changes in target thickness between 500 μm and 1000 μm, and to changes of beam size between 2 mm and 5 mm. The 500 μm target provides a marginal dose-rate increase for the smallest beam size (2 mm) only and the 1500 μm target is everywhere sub-optimal with respect to dose-rate. Hence, the nominal operational conditions comprise a target thickness of 1000 μm to minimize primary electron contamination, while maximizing dose rates, and a 5 mm beam size to keep temperatures in the tantalum low, as will be shown in section 3.2.

The largest impact of changing target thickness is observed in a 'filtration' of the spectrum, predominantly below the pair-production peak at 511 keV (figure 7). A summary of the change in relative energy content for beam spectra produced by the 500 μm and 1000 μm or 1500 μm targets is summarized in table 3, where the energy integral differences are calculated from the energy fluence spectra in figure 7(b). The photon mean energies of the various beam configurations, scored in a 1×1 cm^2 area along the CAX at the location of the phantom surface (at 7.5 cm SSD), are shown in table 4.

Table 3. Integrated 10 MV all-particle energy fluence (relative) differences between target thickness configurations and for various energy ranges [spectral range: <511 keV, >511 keV, or full spectrum]. All spectra were evaluated at the collimator exit (PS#2, figure 4).

	10 MV			8 MV		
[A,B][a]	<511 keV	>511 keV	Full	<511 keV	>511 keV	Full
[500, 1000]	15.36%	−1.11%	−0.47%	10.26%	−1.17%	−0.74%
[1000, 1500]	13.25%	2.05%	2.42%	9.31%	2.02%	3.20%

[a] the spectral differences between the target thickness configurations are calculated as the following integral ratio (R): $R = (A - B)/\max(A,B)$, where A and B are integrals over the energy fluence curves designated by the target thicknesses (in μm) under consideration.

Table 4. Mean photon beam energies for a 1 × 1 cm^2 collimated field evaluated at the phantom surface.

Target thickness (μm)	10 MV	8 MV
500	1.63 MeV +/− 0.05%	1.39 MeV +/− 0.05%
1000	1.76 MeV +/− 0.05%	1.42 MeV +/− 0.05%
1500	1.84 MeV +/− 0.04%	1.56 MeV +/− 0.04%

The 2D dose profiles corresponding to each electron beam size, at the phantom surface and a depth of 1 cm, are shown in figure 8 for a 1000 μm thick target and the 10 MV beam. While smaller beam spots confer an advantage in dose-rate, without increasing the beam penumbra substantially (see table 5), they produce higher thermal stresses within the tantalum layer and are thus detrimental to the converter's design life, as will be demonstrated in the following section.

Figure 9 illustrates the effects of removing the collimator, and thereby allowing for samples to be placed closer to the tantalum target—to within 3.5 cm SSD. The dose maps of figures 9(b), (c) showcase the tradeoff in dose-rate and field conformality at the phantom surface for with and without the 1 × 1 cm^2 collimator at SSDs of 7.5 and 3.5 cm, respectively. The corresponding PDDs are shown in figure 9(d) while the normalized beam half-profiles, which highlight relative changes in the lateral dose distribution, are shown in figure 9(e). Evidently, the collimator succeeds in forming a 1 cm^2 square field size comprised of dose-rates >40 Gy s^{-1}, as required, with only a slight (~1 mm) broadening at the nominal 1 cm treatment depth. The open field, on the other hand provides peak dose-rates in excess of 600 Gy s^{-1}, but with significant beam broadening and an increased depth-dose gradient. For example, at 1 cm depth the gradients are found to be $d\dot{D}/dx = -22.7$ and -164.7 Gy s^{-1} cm^{-1} for the collimated and open-field beams at 10 MV, respectively. At 8 MV these gradients are correspondingly increased to $d\dot{D}/dx = -17.2$ and -135.6 Gy s^{-1} cm^{-1}.

A brief outline of the critical dosimetric performance considerations of the FLASH converter are highlighted in table 6. Clearly, the threshold dose-rate of 40 Gy s^{-1} has been exceeded, even at the nominal SSD (7.5 cm), field size (1 × 1 cm^2) and treatment depth ($z = 1$ cm) for both beam energies, with a clear benefit being demonstrated for using the higher energy (10 MeV) beam for improved bremsstrahlung conversion efficiency and, as will be discussed later, reducing target strain and thus preserving design life.

3.1.1. In vivo *dose distribution using a rodent-morphic 3D-printed mouse phantom*

Figure 10 illustrates the MC-calculated dose distribution in a 3D-printed mouse phantom, validated previously for use in kV treatment beams.

Using the VICTORIA dose visualization application (Badun *et al* 2021), the in-phantom contours are made visible in figure 10(a), while averaged lateral and depth-dose profiles (figures 10(b), (c)) are also included. The dose distributions verify that the beam profile maintains its sharp distribution even at depth and the dose-rate throughout the entirety of the lung (the target organ of interest) remains well above 40 Gy s^{-1} and is expected to be compatible with treatment times of 10^{-2} s to facilitate single-fraction treatments customary of small-animal FLASH experiments which have been conducted to-date (Bourhis *et al* 2019, Montay-Gruel *et al* 2021).

3.1.2. Simulated converter activation, prompt and residual doses

The total equivalent dose at a distance of 0.5 m from the tantalum target, assuming no self-attenuation of the emitted radiations following 1 week of CW irradiation at 1 kW and 10 MeV, is summarized in table 7. It should be noted that neutron radiation transport is considered in the activation analysis and converter energy deposition studies performed with FLUKA, but is not available in EGSnrc MC simulations. Due to our simplifying, albeit conservative, assumption of isotropic emission, the dose can be scaled to any arbitrary distance with an inverse-square correction to the tabulated values.

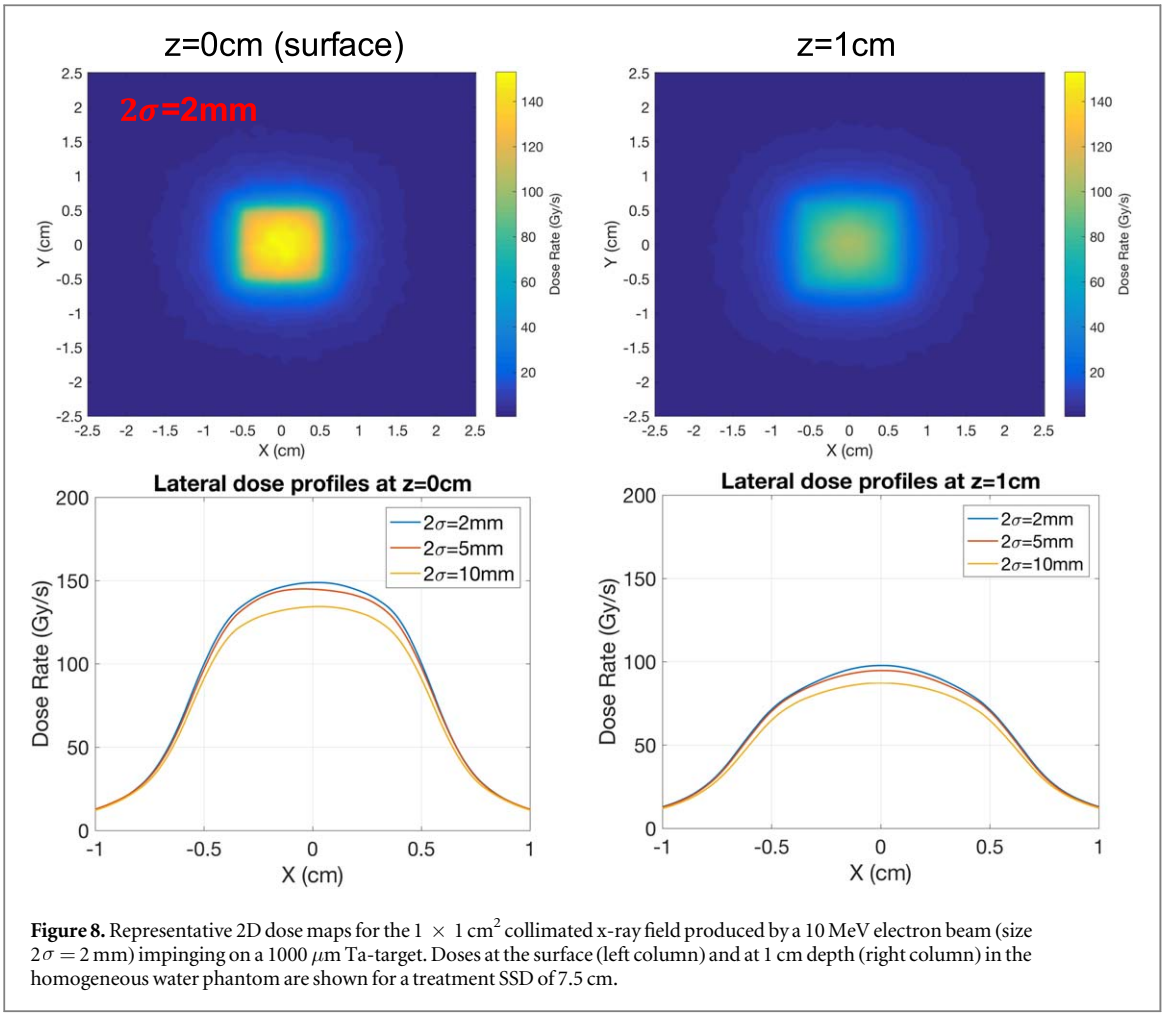

Figure 8. Representative 2D dose maps for the 1 × 1 cm^2 collimated x-ray field produced by a 10 MeV electron beam (size $2\sigma = 2$ mm) impinging on a 1000 μm Ta-target. Doses at the surface (left column) and at 1 cm depth (right column) in the homogeneous water phantom are shown for a treatment SSD of 7.5 cm.

Table 5. 80–20 beam penumbra (in mm) for all electron beam sizes for the 1 × 1 cm^2 collimated 10 MV beam at 7.5 cm SSD. The values in square brackets correspond to the FWHM (in cm) for the same beam profiles.

	80%–20% penumbra (mm) [FWHM (cm)]	
2σ beam size (mm)	Surface	$z = 1$ cm depth
2	3.012 [1.161]	4.235 [1.256]
5	3.011 [1.141]	4.046 [1.266]
10	3.043 [1.136]	3.984 [1.271]

The primary activation products of interest are ^{180}Ta, produced in the tantalum target through the ^{181}Ta(γ,n)^{180}Ta reaction, along with the photo-fission products ^{185}W and ^{182}Ta produced in the W-collimator. While ^{185}W contributes the highest dose-rate, it only emits low-energy beta particles or gammas from the metastable state, whereas ^{180}Ta and ^{182}Ta, both beta emitters, may exist in metastable states which are capable of producing high-energy (>1 MeV) gamma ray fields. ^{179}Ta and fast-decaying ^{179}W are only produced in negligible quantitates, less than the associated error in yield, while the ^{28}Al produced in the Al-flange itself is another short-lived weak beta emitter. Residual doses, in practice, should be much lower than those quoted in table 7 due to the reduced beam uptime under routine steady-state use, and will become lower still during low-frequency, short duration FLASH experiments. For reference, the worst-case estimate for total equivalent dose under 1 kW CW irradiation amounted to 32 μSv h^{-1} at EoB, if activation in the lead shielding surrounding the platform were also included; therefore, FLASH mode residual doses will always remain below this value. Given that the peripheral lead shielding is setup specific, and much farther from the sample/animal jig when compared with the converter flange, it was omitted for the preceding analysis of table 7.

Considering the short time-scale of FLASH irradiations, prompt doses results for the same simulation geometry were found to produce a very small radiological hazard for occupied areas outside of the electron

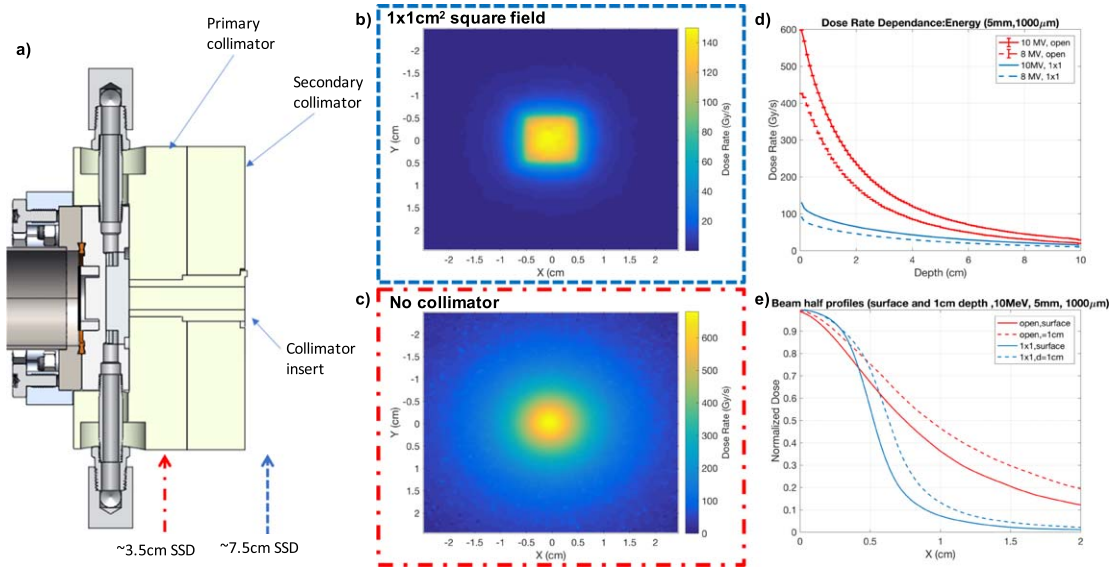

Figure 9. Cutaway model of the modular W-collimator assembly (a) which allows for flexible selection of field size depending on whether the primary and secondary collimators are mounted. A set of 3D-printed tungsten inserts can allow for custom field shaping or flattening filter insertion based on use-case. The collimated (b) and open (c) fields are illustrated to showcase the dose-rate enhancement afforded by the latter. The treatment SSD of the open (SSD = 3.5 cm) and collimated (SSD = 7.5 cm) fields is annotated in (a) and color matched to the dose maps (blue = 1 cm^2; red = open). Corresponding PDDs (d) are included for both field types as well as lateral half-profiles (e) at depths of 0 cm and 1 cm in the water phantom, for which the dose is normalized to the maximum dose for that depth.

Table 6. Primary dosimetric goals for the FLASH converter and simulated results for a 1×1 cm^2 x-ray field size and 1 kW average electron beam power.

Parameter	Goal	Calculated
FLASH dose-rates		10 MV: 84 Gy s^{-1}
(7.5 cm SSD, 1 cm depth in water)	>40 Gy s^{-1}	8 MV: 59 Gy s^{-1}
Primary e- transmission	<0.001%	<0.0006% ($t_{Ta} > 500$ μm)

accelerator hall, with the most severe conditions corresponding to 6.2 μSv h^{-1} when operating the beam in CW mode for beam diagnostics at 200 W and 10 MeV. The equivalent prompt dose-rates scale with beam power and uptime, while beam quality remains the same, and thus the corresponding dose during FLASH mode would reduce to 2 μSv h^{-1} assuming a maximum of 4 FLASH macro-pulses per minute, in order to allow thermal stabilization between pulses.

3.2. FEA thermal and structural simulations of the electron-to-photon converter

This FLASH target will be used in two operational modes:

1) FLASH—during FLASH experiments, a maximum beam power of 1 kW will impinge on this target for a maximum of one second with maximum electron beam energy of 10 MeV.
2) Diagnostic—during regular electron linac development, the electron beam can be delivered to the converter with a maximum power of 200 W for indefinite time.

The 1 s upper-limit to the FLASH operational mode is consistent with the above-mentioned total irradiation times customary of FLASH and also presents the most severe thermal condition expected for our targets. Practical irradiation times will be less than a full 1 s and therefore the implications of varying the irradiation time, assuming a 100% duty factor, on the temperature distribution within the target flange have also been presented in the forthcoming section. The need to preserve beam dump functionality using a low-power CW beam for

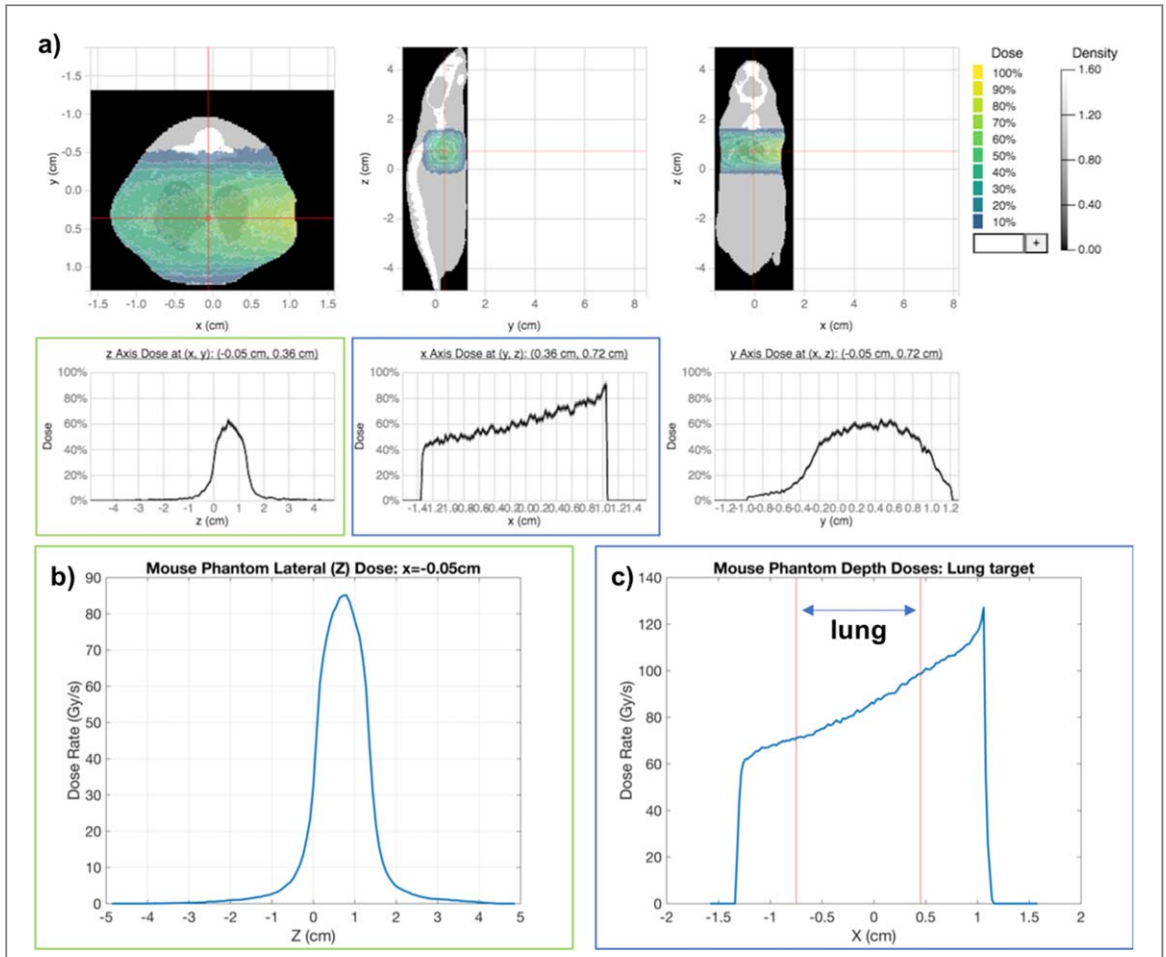

Figure 10. Doses to a realistic 3D-printed mouse phantom visualized using the web-based VICTORIA dose-viewer (a). Note that 100% dose here corresponds to an absolute maximum dose-rate of 142.4 Gy s^{-1}. Area-averaged (0.5 cm^2) lateral (b) and depth dose-rate profiles (c) are shown for the 1 × 1 cm^2 10 MV x-ray beam generated by using a 1 kW, 5 mm electron beam and a 8 cm source-to-surface distance. The lung region of the averaged depth-dose (c), here delineated along the *X*-axis, showcases ultrahigh dose-rates (>40 Gy s^{-1}) throughout the entire organ and is of relevance to planned lung irradiation studies using this MV source.

Table 7. Summary of activation products within the various converter components and the resulting equivalent dose-rates (in μSv h^{-1}) at a distance of 0.5 m from the target. The target is considered as the point source for decay radiations and self-attenuation is omitted. Radioactive decay of the long-lived products is demonstrated through the dose-rate evolution at various times following end-of-beam (EoB).

	EoB	5 m	1 h	1 d	10 d	100 d
Tantalum						
^{180}Ta	8.56	8.50	7.87	1.11	1.18E-8	0
W shield						
^{179}Ta	1.10E-01	1.11E-01	1.11E-01	1.11E-01	1.10E-01	9.99E-05
^{182}Ta	9.35E-01	9.35E-01	9.35E-01	9.29E-01	8.80E-01	5.11E-01
^{179}W	5.77E-02	5.25E-02	1.88E-02	1.15E-13	0	0
^{181}W	4.27E-01	4.27E-01	4.27E-01	4.25E-01	4.04E-01	2.41E-01
^{185}W	1.29	1.29	1.29	1.28	1.18	5.12E-01
Al flange						
^{28}Al	3.02E-01	6.46E-02	2.72E-09	0	0	0
TOTAL	11.6	11.3	10.5	3.75	2.46	1.26

arbitrarily long time periods provided unique requirements for our design, independently of the FLASH mode, and thus steady-state results for the diagnostic mode are also included here.

3.2.1. Summary of steady-state (diagnostic mode) and transient (FLASH mode) thermomechanical results

Figures 11 and 12 highlight the temperature, von Mises stress distributions within the flange for the steady-state (figure 11 CW mode) and transient (figure 12, FLASH mode) simulations, respectively. An extended data set

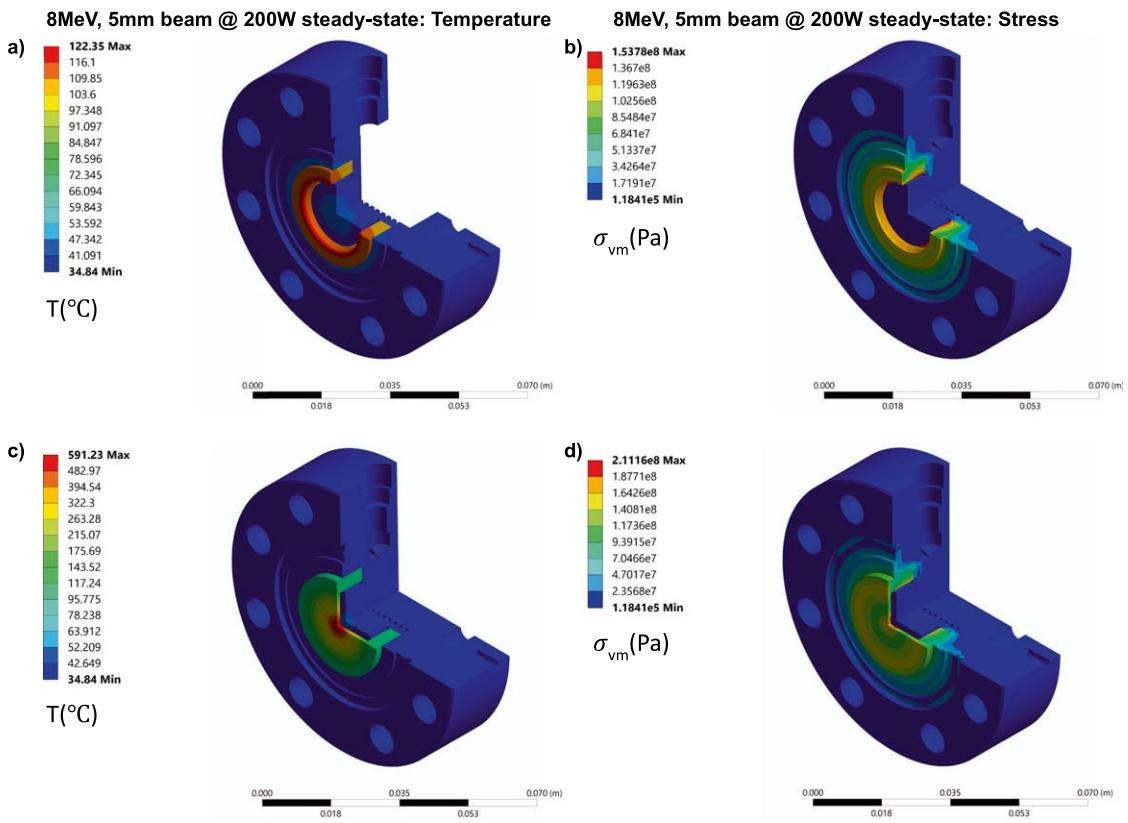

Figure 11. Summary of steady-state ANSYS® FEA simulation results for the 8 MeV CW beam with a 5 mm electron beam size and 200 W average power. The temperature (T) (a), (c) and von Mises stress (σ_{vm}) (b), (d) distributions are shown in aluminum-only (a), (b) and full target (c), (d) views.

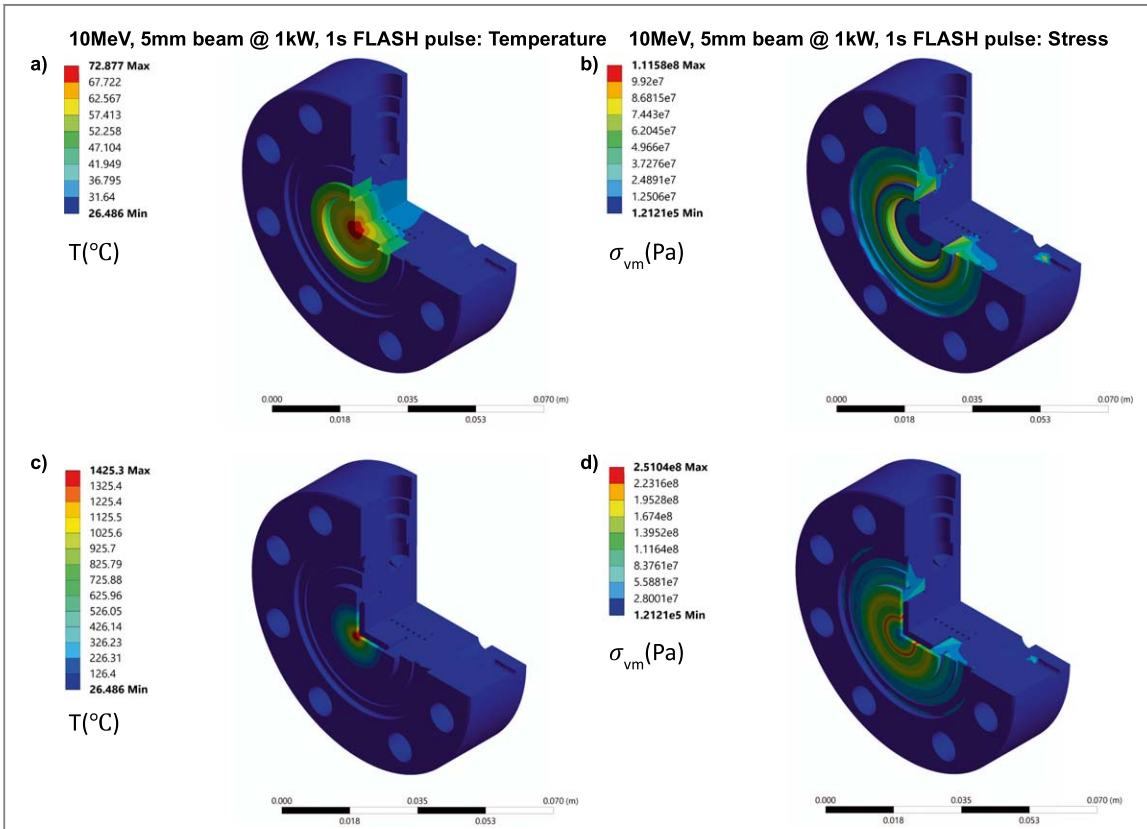

Figure 12. Summary of transient ANSYS® FEA simulation results for the 10 MeV FLASH (pulsed) beam with a 5 mm electron beam size and 1 kW average power operating for 1 s. The temperature (T) (a), (c) and von Mises stress (σ_{vm}) (b), (d) distributions are shown in aluminum-only (a), (b) and full target (c), (d) views. All data are generated at the end of a 1 s electron beam pulse.

Table 8. Elastic and plastic strain components for 200 W steady-state and 1 kW transient simulations for the reference simulation using a 5 mm electron beam size and 1000 μm target thickness. Transient data are sampled at 1 s, the time of simulated beam OFF in FLASH mode.

Beam type	Elastic strain (Al, max)	Plastic strain (Ta, max)	Total (max)
200 W steady-state (8 MeV)	0.0022	0.0028	0.0038
1 kW transient (8 MeV)	0.00559	0.0574	0.0579
1 kW transient (10 MeV)	0.0062	0.0435	0.0439

Table 9. Fatigue analysis for the life-limiting Al components in 8 MV CW beam configurations using a 1000 μm target and for each electron beam size (2σ). The 8 MV case is the most conservative for this fatigue analysis and hence is presented here. S_u and S_y, the ultimate tensile strength of equation (2) for Al-6061 and the yield stress, respectively, are temperature dependent[a].

2σ	Power (W)	Temp (°C)	S' (MPa)	S_m (MPa)	S (MPa)	S_y (MPa)	S_u (MPa)	N (cycles)
10	250	146	196	125	422	217	237	1981
	200	123	159	107	292	239	264	5460
5	250	145	192	123	406	218	239	2192
	200	122	154	104	278	240	265	6378
2	250	149	188	121	2533	214	234	35
	200	125	153	104	275	238	261	6584

[a] S_u and S_y data are interpolated from tables taken from the ASM handbook (ASM International Handbook Committee 1991). For added conservatism, the value of S_u used in equation (2) is taken as the lower of two bounding values for any given temperature rather than the interpolated value shown here—i.e. if $T_{sim} \in (T_{ASM,1},\ T_{ASM,2})$ then $S_u(T_{sim}) = S_u(T_{ASM,2})$.

which includes the elastic strain (relative deformation) may be found in the supplementary material (Figures S1, S2 (available online at stacks.iop.org/PMB/67/105003/mmedia)). For steady-state simulations, a more conservative beam energy of 8 MeV was considered as it induced higher temperatures and stresses in the aluminum components near the tantalum interface, due to the higher power deposition per unit length. To aid in clarity of presentation, the top rows (a), (b) in each figure highlight the aluminum components only, which feature lower extrema compared to the target, which is included in the bottom figure rows (c), (d). It should be noted that plastic strain within the flange (not shown) was non-zero within the tantalum target, but localized to the beam impingement region only; for reference, the maximum values of plastic strain in the tantalum are also summarized in table 8.

According to the von Mises yield criterion, wherever the von Mises stress exceeds the material yield strength, the material will begin to yield plastically (i.e. deform irreversibly). The maximum elastic and plastic strains derived from the calculated stresses are summarized in table 8. Importantly, the degree of deformation in aluminum everywhere remains elastic, while plasticity in tantalum is deemed tolerable based on the ductility characteristics reported in the literature for the temperatures observed.

Note that the total strain is not simply the summation of the elastic and plastic components in table 8 values as the distributions are spatially dependent. The largest plastic strains were observed in the case of transient irradiations at 1 kW, as expected, due to the extreme temperatures reached within the tantalum.

A subset of the fatigue analyses, with the number of cycles to failure (N), is presented in table 9. It includes the ANSYS peak alternating stresses, the mean stress—accounting also for the estimated shrink-fit pre-stress of 50 MPa and 17 MPa on the inner (plug) and outer (flange) cylindrical surfaces of the interference interface—and corresponding Goodman mean-stress corrected stress amplitude for use with equation (2).

The two power values compared in table 9 (200, 250 W) help to demonstrate the detriment of using higher beam power due to the increased stress amplitudes and higher mean stresses experienced over the many steady-state thermal cycles (i.e. beam ON until beam OFF) that are required of the CW (diagnostic) mode. It would be reasonable to operate a CW beam at an electron beam power of 200 W or lower, for beam sizes larger than 2 mm, assuming a design-life requirement of 3000 thermal (beam) cycles over 5 years of operation. The selection of 200 W as the benchmark steady-state power follows from this fatigue evaluation for the CW electron beam of the ARIEL e-linac, which is typically employed during routine beam development.

The ANSYS tantalum fatigue results yielded values of N in excess of 10^4 under the same conditions and are therefore not included in the design life analysis for steady-state operation. For 1 kW FLASH irradiation at 10 MeV, however, the length of beam ON has a drastic impact on the life of the tantalum due to the rapid heating and extreme temperatures; importantly, the value of N for the 5 mm beam decreases from 16 310 at 0.1 s (max $T_{Ta} = 557$ °C) to 811 at 1 s, where the maximum T_{Ta} can reach 1425 °C, based on conservative thermal parameters (table 2).

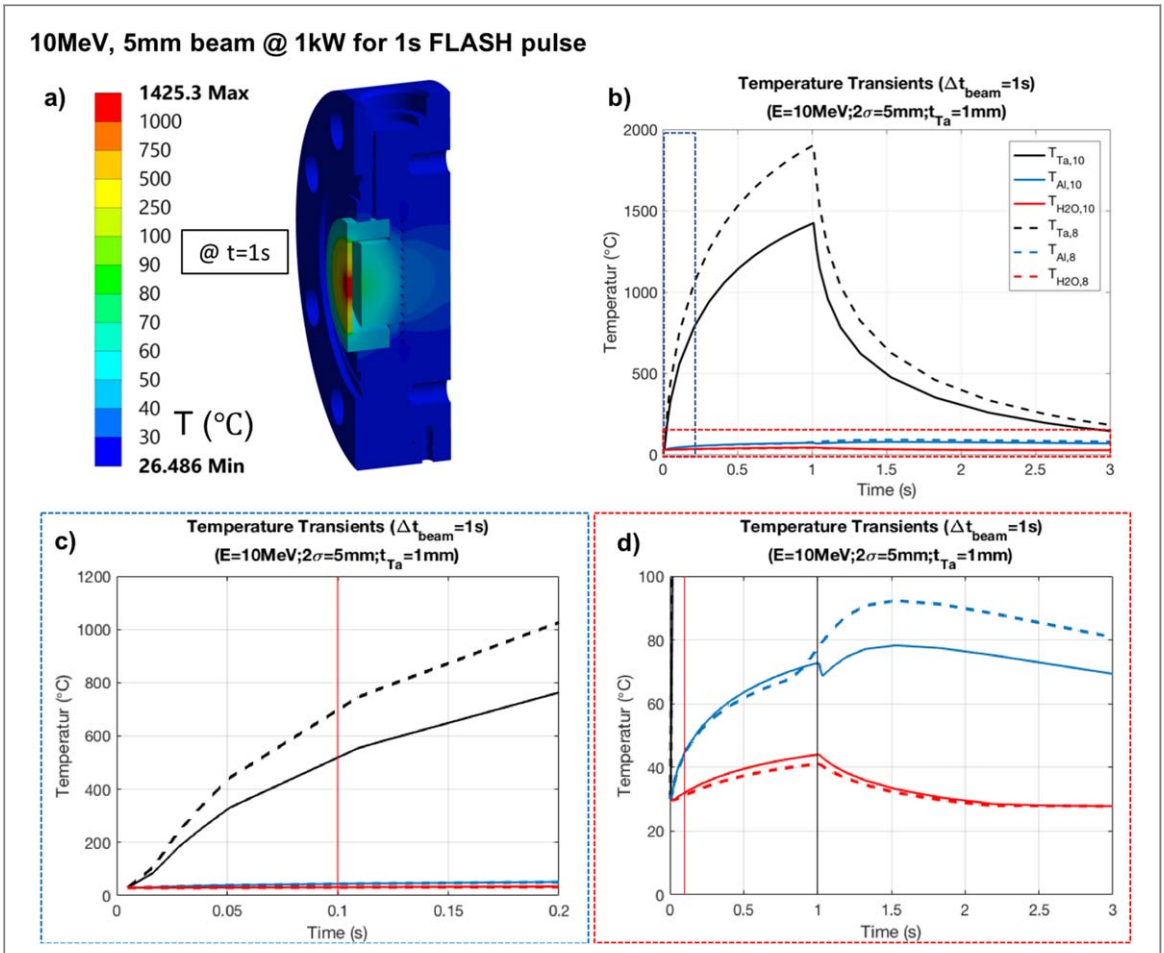

Figure 13. Transient temperature evolution of the 5 mm, 10 MeV FLASH reference beam. The FEA result (a) samples this data at $t = 1$ s. A non-linear colorbar scale is used to visualize the beam-induced heating across the converter CAX. The temperatures in each of the converter materials are plotted as a function of each time step in (b). Ta temperature evolution on short (<0.2 s) timescales (c) and the comparatively cool Al and water bodies (d) are also brought into focus.

The detailed temperature evolution of the 10 MV, 1 kW transient (FLASH mode) irradiations are shown in figure 13 for the 5 mm electron beam size.

The temperature time-evolution over 100 ms, a timescale of interest for FLASH-RT, is visualized in figure 13(c). The extremely rapid heating rate within the Ta as compared to the aluminum and water channels, which exhibit comparatively slow temperature variations over time, demonstrates the ability of the flange to remove the deposited heat as it equilibrates (figure 13(d)). Whereas T_{Ta} increases to 1425 °C or 1905 °C within 1 s of beam ON at 10 MeV and 8 MeV, respectively, the conductive aluminum corona only sees a corresponding increase of 45 °C–49 °C within that same period. 8 MeV results here reaffirm the benefit to using higher beam energy from a thermal perspective, namely to achieve lower peak temperatures and smaller gradients in the tantalum and aluminum components which lend to lower stress rates, thermal strain and thus a longer life for the Ta target layer.

3.2.2. Overview of thermomechanical design limits and calculated extreme values

An overview of the thermomechanical design limits and the calculated values are shown in table 10. All goals were met and, together with achievement of the dosimetric performance goals outlined in table 6, constitute a full acceptance criteria for the prototype fabrication, which has since been successfully completed.

4. Discussion

The ARIEL converter flange is being developed to provide an ultrahigh dose-rate (UHDR) x-ray source, suitable for FLASH radiobiological experiments, based on the conversion of the high powered electron beam delivered by the ARIEL e-linac. This achievement requires a target that is capable of withstanding high instantaneous power (1 kW) over many thermal cycles for UHDR irradiations while routinely serving as a diagnostic beam dump under lower-power (200 W) steady-state (CW beam) irradiation—a unique requirement of our platform.

Table 10. Mechanical design limits and simulated results of the final converter prototype. Stress–strain limits are evaluated for the 8 MeV steady-state (SS) beam while transient temperatures (FLASH) are evaluated after a full 1 s FLASH mode irradiation in order to represent the most intensive conditions for each parameter to afford a more conservative design.

Parameter[a]	Mode	Design limit	Calculated
T_{Ta}	FLASH (transient)	<2000 °C	<1905 °C
T_{Al}	SS	<200 °C	<122 °C
T_{H2O} (channel interface)	FLASH	<100 °C	<60 °C
Ta plastic strain	SS	<0.02	<0.005
Al plastic strain	All	<0.02	~0
SS design life—steady-state (N cycles before failure, Al)[b]	SS	>3000	>6000 @ 200 W

[a] Peak temperatures are evaluate for the transient 8 MeV, 1 kW beam simulations at $t = 1$ s using a 5 mm electron beam size and 1000 μm target. This represents the nominal FLASH mode treatment beam configuration under the more intensive thermal conditions afforded by the lower beam energy.

[b] The target design life is limited by the aluminum parts in the case of a 200 W steady-state beam.

MC and FEA thermomechanical simulations have been used to inform flange optimization directly using an iterative design framework (figure 1). Reasonable design limits were set based on dosimetric and thermal performance goals which must be simultaneously met along with acceptable manufacturing practices. Moreover, the dosimetric performance during UHDR (FLASH mode) irradiations had to be evaluated within practical and thermomechanical constraints identified for safe operation of the target during steady-state (diagnostic mode) irradiation. A prototype converter based on a design informed through the methodology presented here has since been fabricated.

The final target prototype leverages a novel thin-target design motivated by the need to implement a small (space-saving), thermally efficient and static photon converter. High thermal and mechanical stresses are inevitably generated within the converter as a result of the enormous thermal load deposited by the impinging high-energy electron beam. To remove heat from the system, the high-Z bremsstrahlung target requires reliable and persistent contact with an actively water-cooled backing material. This was facilitated by interfacing Al-6061 with a tantalum target layer using explosion bonding (welding) processes which maximizes heat conduction across the laminated Ta–Al interface. In order to limit temperatures in the aluminum, especially at the interfacial boundary, the bonded aluminum within the region of e-beam impingement was removed, thereby creating an aluminum cylindrical interface (corona) axially bonded to the tantalum 'window' (figures 3(a), (b)). In order to realize this design, without creating water-leak paths into the ARIEL particle-free ultra-high vacuum (UHV) beamline, the target was assembled by adopting a two-piece shrink fitting approach whereby the bonded Ta–Al layer was fashioned into a 'plug', cooled in liquid nitrogen, and inserted into the water-cooled Al-6061 flange (figure 3(c)). The subsequent expansion (at room temperature) within a precision machined flange creates a contact interference between 5 and 26 μm whichaffords excellent thermal conductance across the aluminum-to-aluminum (coronal to flange) interface, limited predominantly by the microscopic surface roughness (65 micro-inches RMS) and manufacturing (i.e. cylindricity) tolerances. A higher conductance leads to reduced temperatures and thermal strain, thereby offering improved target longevity as well as a potential to deliver higher power and, in turn, increased dose-rates.

The use of the Ta-window design has helped to reduce the stresses at the critical Ta–Al interface and no plastic deformation, a key factor in the low-cycle design life, was observed within the simulated aluminum geometries. Secondly, the robustness of the explosion bonded Ta–Al joint was inferred from literature. In the previous work by Egoriti *et al* (2020), a sample of explosion-bonded tantalum to Al-6061 was irradiated with an electron beam at 300 keV at the ARIEL converter test stand (CTS) (Egoriti *et al* 2020). The temperature and stresses resulting from this reference test at the Ta–Al interface were higher than those seen in the FLASH converter; hence, the delamination risk from the design presented in this work was considered to be retired.

Other notable modifications to the converter include a 1 mm diameter vacuum pumping port, which was added to allow for degassing within, and evacuation of, the vacuum pocket during bake-out, while simultaneously reducing the pressure differential across the tantalum target layer (figure 3(b)). Maintaining UHV within the vacuum pocket also minimizes the risk of oxygen exposure at the interior tantalum surface, which can otherwise lead to target oxidation and embrittlement, which would pose and as yet uncertain detriment to target life. The precipitation hardened 6061 flange body (T6 re-tempered) was selected for its resistance to erosion-corrosion effects and the improved tensile strength of the T6 condition, both of which help to maintain a leak-free connection to the rest of the steel beamline. It should be noted that the effects of radiation embrittlement may be of relevance to a thin target design, but were beyond the scope of this work. Fortunately, tantalum targets have previously been found to remain ductile even after prolonged periods of intense,

high-energy irradiation using heavier particles capable of imparting substantial recoil energy to the knock-on atom precursors of damage cascades within the target material (Wilcox 2016, Ophoven *et al* 2021). While the literature on this subject is sparse, successful multi-year operating experience, for example with tantalum clad ISIS targets, may imply a reasonable preservation of thin Ta-targets even in the absence of a dedicated study on electron irradiation-mediated damage (Wilcox 2016, 2018). The aforementioned ARIEL CTS results at TRIUMF have also reaffirmed the robustness of Ta–Al explosion bonded targets in UHV conditions whereby experimental evidence failed to demonstrate radiation-damage assisted failure modes in the target, even at high operating temperatures ($T_{\mathrm{max,Ta}} = 658$ °C; $T_{\mathrm{max,Al}} = 236$ °C) under CW irradiation over long time periods (500 h, 50 cycles) (Egoriti *et al* 2020).

Since a primary goal of target optimization was to maximize dose-rates, the results indicated that the small target thicknesses might be preferable due to the higher surface dose-rates and loss of build-up owing primarily to secondary electron dose (figure 5). However, these observations had to be made considering the requirement that we must stop all primary electrons in the target (table 6), a condition which was not met for the 500 μm target. Bearing this electron transmission constraint in mind, the optimal target thickness was selected to be 1000 μm, as it maximized the dose rates at all depths while mitigating primary electron transmission at 10 MeV, as demonstrated in figure 5(b). Moreover, allowing the tantalum layer to be as thick as possible, without compromising dosimetric performance, improved its mechanical resistance against stresses and corrosive buildup of surface oxide layers that may occur at high temperatures. Due to manufacturing constraints and the surface defects which follow the explosion-bonding process, thickness tolerances below 500 μm would be difficult to realize and this in turn supported a coarser optimization of target thickness using increments of 500 μm.

While it lies beyond the intended application scope of the FLASH converter, a surface dose enhancement may provide an interesting opportunity for those interested in mixed radiation beams; in that case, it would be possible to greatly increase doses down to a depths <1 cm using thinner targets and by exploiting the primary-electron dose deposition. For the thicker targets (>1000 μm), on the other hand, the contaminant electron dose is derived from secondaries generated in the flange and the W-collimator (figure 5(b)), exacerbated by their close proximity (CSD $<$ 5 cm) to the water phantom. For the 1000 μm target and 5 mm beam size, secondary electrons generated in the 10 MV field contribute up to 72% of the surface dose, quickly decaying to <10% at $z = 1$ cm depth and <2% by $z = 2$ cm; contributions are reduced at 8 MV for all depths in water. Superficial dose due to these low-energy electrons ($\bar{E}_{10MV} = 1.3$ MeV) should therefore be taken into consideration for *in vivo* surface dosimetry or where measurement devices mounted on the irradiation jig may be irradiated (i.e. at SSD $=$ 7.5 cm). Our simulated beam is somewhat unique in that it delivers MV x-rays while avoiding a superficial build-up region where dose-rates might otherwise fall below a UHDR threshold for FLASH, which we assumed here to be 40 Gy s^{-1}. This depth-dose feature is shared by synchrotron (kV) x-ray or low-energy electron FLASH sources used to date, but the implications of using mixed low-energy electron and MV photon beams for the FLASH effect have not been studied. Additionally, the mixed field might pose challenges for accurate dosimetry. Design modifications to accommodate thinner targets could be relevant for lower-energy beams better suited to other UHDR applications, especially keV spatially-fractionated modalities such as micro-/mini-beam radiotherapy. However, if these low beam energies are desired, then our 500 μm lower limit for the Ta-target thickness may preclude the use of the target-window design presented here.

Using a higher energy photon beam offered an obvious improvement in dose-rates (figures 5(a), 6(a)) for each target thickness configuration and all beam sizes, even when disregarding the enhanced secondary electron fluence—this can be observed in the depth-dose differences for depths $>$ 1 cm. For example, in figure 5(a) the relative dose-rate difference between 8 and 10 MV beams (normalized to the 10 MV data), for depths >1 cm, ranged between 29% and 34% across all simulated configurations and increased with depth in the water phantom.

The converter together with the collimator assembly has been designed such that >40 Gy s^{-1} could be achieved for a 1 $\times$ 1 cm^2 field size at a nominal SSD of 7.5 cm, as demonstrated in figure 9. This field size was selected as being typical for small-animal irradiators and suitable to mouse lung irradiations for which the ARIEL FLASH system is being designed (Bazalova *et al* 2014). However, because of the W-collimator modularity, it can also accept a number of 3D-printed inserts with common form factors, as long as they fit within the 2 cm diameter aperture of the secondary collimator, which itself defines the largest field size (see figure 9(a)). Alternatively, the primary and secondary collimators can be removed from the beam path entirely. This latter configuration might be of interest, for example, where exceptionally high dose-rates (>600 Gy s^{-1}) are required without the need for field conformality, possibly outside of small-animal experiments. Removal of all collimators (open beam) was found to increase the available dose-rate by a factor of 4.56 and 4.62 for the 10 and 8 MV beams ($2\sigma = 5$ mm, 1000 μm thick target), respectively, at the minimum SSD of 3.5 cm. Optimizations for improved field conformality and transversal characteristics are being considered for future

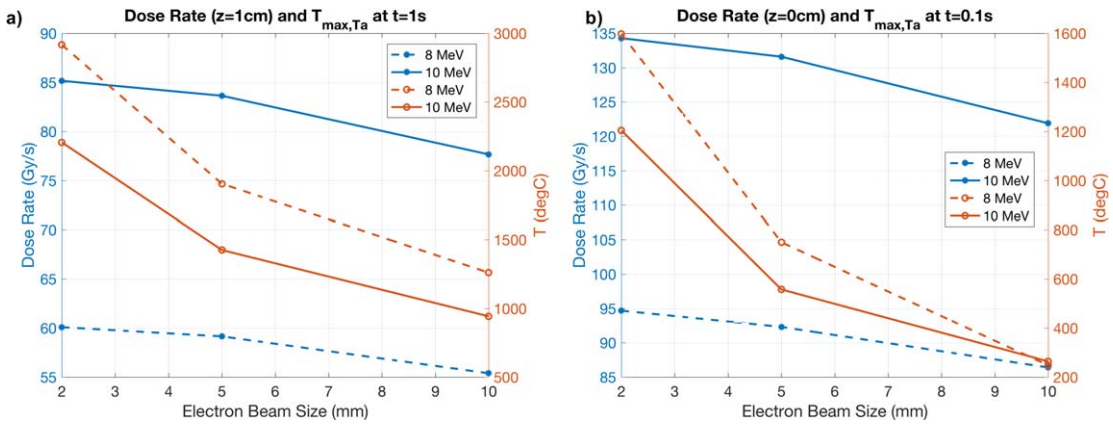

Figure 14. Combination plots for simulated dose-rate and peak Ta temperatures (T_{Ta}) for the 1 × 1 cm^2 FLASH-mode treatment x-ray beam. A Ta-target thickness of 1000 μm is simulated with an average beam power of 1 kW at 8 MeV (0.125 mA) and 10 MeV (0.1 mA). Data are shown for a full 1 s irradiation at a depth (z) of 1 cm in the water phantom (a), reflecting a more extreme set of conditions which were compared against the design goals. Data evaluated at the phantom surface for a typical FLASH irradiation time of 0.1 s is also included (b) to reflect a superficial treatment scenario.

collimation strategies; for example, we are considering 3D-printed flattening filters to compensate and flatten the x-ray field.

Given that the dose attributable to both contaminant electrons and x-rays at the surface of small-animal models may have dosimetric implications, the transport of the electrons through the entire aluminum flange had to be considered. This was necessary to accurately model the secondary electron shower and promote bremsstrahlung x-ray production within the flange itself. To this end, the electron transport threshold for the BEAMnrc simulations was set to a low value of 150 keV and electron range rejection was not employed. As an example, the mean electron energy upon exiting the aluminum flange (SSD = 2 cm) was approximately 1.5 MeV, at which point the radiative yield is 13.7% of that in tantalum at the same energy, and this value increases for the higher energy electrons which enter the flange after the Ta target.

To ensure that the performance of the system meets the prescribed design goals (tables 6 and 10), the quantities of interest, namely UHDR dose-rates and converter temperatures, were evaluated under a conservative set of assumptions. From a thermomechanical perspective, important heat transport parameters were reduced by a safety factor of 2 in order to assure operation at 1 kW remained tenable. Furthermore, treatment dose-rates were evaluated against the threshold (40 Gy s^{-1}) at a depth of 1 cm in water, which is of relevance to planned small-animal irradiations. The maximum target temperatures, meanwhile, were evaluated after a full 1 s of irradiation, despite the expected beam ON time for a typical FLASH biological irradiation being an order of magnitude less (~100 ms). This increased time to beam OFF (1 s) has the important implication that the corresponding thermomechanical results reflect a more extreme, but less likely, operating condition compared to that of a 0.1 s long irradiation, as evidenced by the large temperature increase, from 510 °C to 1425 °C at 10 MeV, between 0.1 s and 1 s total irradiation times (figure 13).

The combined results of the MC and FEA simulations are illustrated in figure 14. The improved dose-rates and reduced peak tantalum temperatures are immediately evident at higher beam energy together and with beam sizes >5 mm.

The results of the combined MC and transient FEA simulations (figure 14) illustrate that the design goals (tables 6 and 10) have been met, with the added margin of safety discussed above. There were clear benefits to dose-rate from selecting the higher beam energy, besides the improved depth of penetration, as previously noted (see figure 6). For example, using an electron beam energy of 10 MeV and spot size of 5 mm, the dose rates could be increased by up to 41.4% relative to an 8 MeV beam of the same size and power at 1 cm depth, while generating transient tantalum peak temperatures (T_{Ta}) which were a factor of 25.7% lower after 1 s (figure 14(a)). Use of smaller beam sizes, meanwhile, appeared beneficial for increasing peak dose-rate, due largely to geometric factors improving transmission of forward-directed x-rays, but with a trade-off in target protection given that T_{Ta} increases substantially due to the increased power density on the tantalum target. For example, in the 10 MeV beam, T_{Ta} increased by 116% in the first 0.1 s when decreasing the beam size from 5 mm to 2 mm, in exchange for a dose-rate increase of only 2.1% (figure 14(b)). The importance of minimizing the peak temperatures while pursuing maximal dose-rates is of critical importance to the viability and longevity of the target design. Altogether, the implication is that for the 1000 μm target using the higher beam energy (10 MeV) together with a 5 mm electron beam size offers the best compromise between dose-rate and peak temperatures at the time scales of interest in FLASH-RT and has become the reference configuration.

In the interest of designing a flange capable of both FLASH (low-cycle) and routine diagnostic (high-cycle) usage, the fatigue life of the converter had to be estimated. The use of safety factors on the life of the material helps to account for and mitigate added risk owing to the design life uncertainty. We estimated that the converter would be capable of surviving at least 6378 cycles under steady-state 5 mm beam irradiation, limited by fatigue in the aluminum corona of the target plug rather than the thin tantalum target itself. This is substantiated by the observation that negligible plastic strain was observed in the tantalum for a 200 W CW irradiation (table 8) and the fact that the ductility of tantalum affords it long life under largely elastic (reversible) cyclic strain (Papakyriacou *et al* 2001, 2002, Nelson 2020). Furthermore, tantalum endurance limits—the fully-reversed stress amplitudes to survive 2×10^8 cycles—are generally higher than the worst-case stress amplitudes reported here at 200 W (table 9), although there may be notable variations depending on the material conditioning and testing frequency (Papakyriacou *et al* 2001, Wilcox *et al* 2018). Under the extreme conditions of FLASH irradiation, by contrast, the impact of increased strain on design life is important under the cumulative damage theory (Campbell 2008) whereby the percent of life expended under FLASH irradiation is carried over to the case of lower power, and less destructive, steady-state operation. Fortunately, the design life for the tantalum target under the 1 kW FLASH mode, assuming that the irradiations are short (~0.1 s), far exceeds that of even the aluminum corona at an estimated 16 310 cycles. However, in the event of an off-normal (>1 s) irradiation at 1 kW, the target life would be reduced due to the extreme temperatures and stresses experienced to approximately 811 cycles. In such a case, it would only take ~405 off-normal exposures to reduce the life by half, the equivalent of running 3189 cycles at 200 W steady-state. These considerations are important to inform accelerator operators about the timeline for replacement and how this may be modified by accidental events.

The converter has been shown to produce a negligible increase in radiological hazards based on activation and prompt doses (section 3.1.2). Activation in the target at 10 MeV is present, but the resulting radioactive isotopes (table 7) together generate equivalent dose-rates at a nominal personnel distance (0.5 m) that would be unlikely to pose a risk, especially considering the short-duration access required of the irradiation platform. Moreover, the calculated values assume no component self-attenuation as well as impractically long CW irradiation at 1 kW, which is not possible given the operational power limit of the flange design (i.e. CW at 200 W only). Activation in the target and collimator geometries are also the primary contributors to non-therapeutic doses to experimental animal models. This is of particular relevance due to the close proximity of the converter to the location of the irradiated sample, device or small animal (in the irradiation jig). The activities and doses in calculated in FLUKA assumed 1 week of continuous CW irradiation at 1 kW, which is unlikely to occur considering the design limitations of the flange, but provides a very conservative estimate to re-affirm the safety of operating the converter under high-powered irradiation using 10 MeV electrons, which are capable of producing a very low neutron flux (Rudd *et al* 2007, Naseri and Mesbahi 2010). The reduced uptime, lower beam power and converter shielding/collimation will together greatly reduce the radiation hazard in spite of the close proximity of small animals restrained by the irradiation jig located at ~7.5 cm SSD.

The target flange will ultimately be used to enable small-animal (rodent) FLASH-RT research at TRIUMF. Along with the provision of UHDR for <1 s single-fraction mono-directional treatments, the field will have qualities that allow for reasonable beam conformality and mean dose-rates above 40 Gy s^{-1} at the nominal treatment depth of 1 cm. MC simulations of a realistic mouse phantom irradiations using the 10 MV treatment beam (1000 μm target, 5 mm 2σ), representative of an experimental lung irradiation (figure 10), were used to illustrate the successful collimation strategy and >40 Gy s^{-1} UHDR delivery at depths throughout the entirety of the mouse thorax that is intersected by the beam (figure 10(c)). The beam was not substantially divergent within the phantom and the requisite dose-rates are achieved in a 1×1 cm^2 field at all depths. A substantial increase in dose-rate can be effected by positioning an animal, or any other sample of interest, near to the converter flange (Al face) without collimation at the expense of the conformality afforded to the collimated fields (figure 9). It is interesting to note that at MeV electron energies the x-ray production efficiency is such that the power requirements for achieving UHDR with our target (~1 kW) are lower when compared to a UHDR functionalized static anode x-ray tube (i.e. 3–6 kW) (Bazalova-Carter and Esplen 2019, Cecchi *et al* 2021) and at least an order of magnitude lower than modern high-performance rotating anode x-ray tubes (60–100 kW) (Schardt *et al* 2004).

The importance of developing a static target design capable of UHDR x-ray irradiation derives from the fundamental difference in the delivery requirements of FLASH-RT compared to conventional dose-rate therapies. Specifically, the sub-second nature of single fraction FLASH-RT is incompatible with conventional, gantry-mediated intensity modulation (IMRT, VMAT) techniques, and instead lends itself well to stationary accelerator beamline and target setups, not unlike the source considered in the present work. To then enable multi-directional intensity modulated fields, the use of multiple beamlines nigh-simultaneously could provide the desired solution; this is the approach proposed for the 10 MV SPHINX system to deliver FLASH RT with MV x-ray beams (Maxim *et al* 2019). To enable such a deliver system, however, each individual beamline target would be required to withstand only a very short, pulsed exposure period compatible with the FLASH-RT

definition (<1 s), rather than using a continuous beam. The robustness against short duration, high-powered pulses of the design presented in this work might therefore be relevant to future development efforts towards UHDR-capable MV bremsstrahlung sources and enabling a clinical translation of x-ray FLASH. To date, only a single demonstration of a MV UHDR x-ray source suitable to FLASH-RT has been published, namely using the PARTER system located at the Chengdu terahertz free electron laser facility (CTFEL; Chengdu, China), which leverages a rotating target to distribute heat deposited by the incident electron beam circumferentially around the target, in a manner similar to a rotating-anode x-ray tube (Gao *et al* 2020). The benefit of instead working towards a static target design relates to the comparative affordability and suitability to compact, multi-directional treatment machines, particularly if combined with electron beam rastering capabilities. However, owing to its rotating target design and lower beam energy, the PARTER system offered depth-dose distributions which were well-suited to small-animal experiments. By comparison, a key limitation of the static target design presented in this work is the steep depth-dose gradient, resulting largely from the use of very short treatment SSDs. In pre-clinical subjects (figure 10(c)) this can manifest as dose non-uniformity and presents a shortcoming when compared to, for example, the PARTER MV x-ray beam or proton beams employing a shoot-through method. This may be of some concern if the treatment dose is at the center of a larger subject requiring over-dosing of the more superficial tissues, possibly beyond a tolerable threshold for toxicity. Similarly, at greater tissue depths this might result in an inability to reach the supposed lower dose threshold required for initiating the FLASH effect while treating shallower sites.

In the course of the ARIEL FLASH project, and following online beam commissioning of the converter presented herein, the authors endeavor to offer a first demonstration of FLASH at this key treatment energy. Higher beam powers, up to 10 kW, may also be possible and limited only by the thermal tolerances of the components associated with the FLASH irradiation station. Conversely, a lower beam power enables conventional (low dose-rate) irradiations on a common platform, using the same experimental conditions and beam spectra. The beam quality is theoretically maintained by modifying the electron beam power, via the duty factor, without the need for retuning of e-linac running parameters. Furthermore, single (macro) pulses with widths between 0.5 and 1000 ms allow for variable instantaneous dose-rates to be delivered in a FLASH-pulse operational mode by setting the duty factor to <100% while maintaining a 1 kW average beam power. The irradiation platform will facilitate a first exploration of FLASH-RT in pre-clinical models using 10 MV x-rays delivered with a static bremsstrahlung target design.

5. Conclusion

A photon conversion target for the high-power ARIEL electron linac at TRIUMF has been successfully designed to satisfy a series of conservative performance thresholds suitable to UHDR irradiations and, eventually, FLASH radiobiological studies. Dose rates in excess of 80 Gy s^{-1} at 1 cm depth in a water phantom were simulated for all beam configurations considered, well above the 40 Gy s^{-1} design lower limit. Meanwhile, temperatures and resulting thermal stresses were everywhere tolerable based on the intended practical limits set according to intended use cases, including total strain and design life requirements, and therefore support the robustness of the final converter design. The prototype is currently being validated/evaluated and will be refined, if needed, following commissioning on the 10 MeV ARIEL electron beam.

Acknowledgments

The authors would like to acknowledge the TRIUMF lab for supporting this developmental work and for provision of its technical and scientific resources, including trained personnel and facilities. In particular, the authors thank Doug Preddy for offering his consistent technical support and expertise to the project. We also thank Chris Secord, Mike Wicken and the TRIUMF machine shop for their practical inputs and target fabrication, Jericho O'Connell of the UVic XCITE lab for work on the motion stage apparatus, and the UVic Center for Advanced Materials and Related Technology (CAMTEC). This work was funded in part by NFRF (NFRFE-2018-00102) and NSERC Discovery grants as well as the Canada Research Chairs program.

ORCID iDs

Nolan Esplen https://orcid.org/0000-0002-8347-8653
Luca Egoriti https://orcid.org/0000-0002-9998-5393
Cornelia Hoehr https://orcid.org/0000-0002-3961-5470

References

Ames F *et al* 2016 The TRIUMF ARIEL RF modulated thermionic electron source *Proc. 28th Linear Accel. Conf. LINAC 2016* pp 310–2

ASM International Handbook Committee 1991 *Properties and Selection: Nonferrous Alloys and Special-Purpose Materials* vol 2 (Materials Park, OH: ASM International)

Badun E, Tessier F, Townson R, Mainegra-Hing E, Storey M-A and Bazalova-Carter M 2021 Introducing the Voxel Interactive Contour Tool for Online Radiation Intensity Analytics (VICTORIA) arXiv:2105.14145 pp 1–5

Barzelay M E, Tong K N and Holloway G F 1955 *Effects of Pressure on Thermal Conductance of Contact Joints (TN-3295)* (Washington: NACA)

Bazalova M, Nelson G, Noll J M and Graves E E 2014 Modality comparison for small animal radiotherapy: a simulation study *Med. Phys.* **41** 5–7

Bazalova-Carter M and Esplen N 2019 On the capabilities of conventional x-ray tubes to deliver ultra-high (FLASH) dose rates *Med. Phys.* **46** 5690–5

Bechtold J H 1955 Tensile properties of annealed tantalum at low temperatures *Acta Metall.* **3** 249–54

Beyreuther E, Brand M, Hans S, Hideghéty K, Karsch L, Leßmann E, Schürer M, Szabó E R and Pawelke J 2019 Feasibility of proton FLASH effect tested by zebrafish embryo irradiation *Radiother. Oncol.* **139** 46–50

Bourhis J *et al* 2019 Clinical translation of FLASH radiotherapy: why and how? *Radiother. Oncol.* **139** 11–7

Buonanno M, Grilj V and Brenner D J 2019 Biological effects in normal cells exposed to FLASH dose rate protons *Radiother. Oncol.* **139** 51–5

Campbell F C 2008 *Fatigue Elements of Metallurgy and Engineering Alloys* (Materials Park, OH: ASM International)

Cecchi D D, Therriault-Proulx F, Lambert-Girard S, Hart A, Macdonald A, Pfleger M, Lenckowski M and Bazalova-Carter M 2021 Characterization of an x-ray tube-based ultrahigh dose-rate system for *in vitro* irradiations *Med. Phys.* **48** 7399–409

Darafsheh A, Hao Y, Zwart T, Wagner M, Catanzano D, Williamson J F, Knutson N, Sun B, Mutic S and Zhao T 2020 Feasibility of proton FLASH irradiation using a synchrocyclotron for preclinical studies *Med. Phys.* **47** 4348–55

Davis J R 2001 *Tantalum and Tantalum Alloys* (Materials Park, OH: ASM International)

Egoriti L, Cervantes M, Day Goodacre T and Gottberg A 2020 Material development towards a solid 100 kW electron-gamma converter for TRIUMF-ARIEL *Nucl. Instrum. Methods Phys. Res. B* **463** 232–6

Esplen N, Alyaqoub E and Bazalova-Carter M 2019a Technical note: manufacturing of a realistic mouse phantom for dosimetry of radiobiology experiments *Med. Phys.* **46** 1030–36

Esplen N and Egoriti L 2020 Developing a spatially-fractionated FLASH-RT x-ray platform *WIMP2020 (Breckenridge, CO, USA)*

Esplen N, Mendonca M S and Bazalova-Carter M 2020 Physics and biology of ultrahigh dose-rate (FLASH) radiotherapy: a topical review *Phys. Med. Biol.* **65** 23TR03

Esplen N, Therriault-Proulx F, Beaulieu L and Bazalova-Carter M 2019b Preclinical dose verification using a 3D printed mouse phantom for radiobiology experiments *Med. Phys.* **46** 5294–303

Farrell K, Schaffhauser A C and Stiegler J O 1967 Recrystallization, grain growth and the ductile-brittle transition in tungsten sheet *J. Less-Common Met.* **13** 141–55

Favaudon V *et al* 2014 Ultrahigh dose-rate FLASH irradiation increases the differential response between normal and tumor tissue in mice *Sci. Transl. Med.* **6** 245ra93

Gao F *et al* 2020 First demonstration of the FLASH effect with ultrahigh dose rate high-energy X-rays *Radiother. Oncol.* **166** 44–50

Girdhani S *et al* 2019 FLASH: A novel paradigm changing tumor irradiation platform that enhances therapeutic ratio by reducing normal tissue toxicity and activating immune pathways *Cancer Res.* **79** LB–280

Ho C Y, Powell R W and Liley P E 1974 Thermal conductivity of the elements *J. Phys. Chem. Ref. Data* **3** 279–421

ICRU 1989 *Tissue Substitutes in Radiation Dosimetry and Measurement (ICRU Report 44)* (Bethesda, MD: International Commission on Radiation Units and Measurements)

Incropera F P and DeWitt D P 2002 *Fundamentals of Heat and Mass Transfer* (Hoboken, NJ: Wiley)

Jaccard M, Durán M T, Petersson K, Germond J F, Liger P, Vozenin M C, Bourhis J, Bochud F and Bailat C 2018 High dose-per-pulse electron beam dosimetry: Commissioning of the Oriatron eRT6 prototype linear accelerator for preclinical use *Med. Phys.* **45** 863–74

Jorge P G *et al* 2019 Dosimetric and preparation procedures for irradiating biological models with pulsed electron beam at ultra-high dose-rate *Radiother. Oncol.* **139** 34–9

Kim M M *et al* 2021 Comparison of flash proton entrance and the spread-out bragg peak dose regions in the sparing of mouse intestinal crypts and in a pancreatic tumor model *Cancers* **13** 4244

LaForce R, Berning R F and Coffin L F Jr 1971 *High-Temperature, Low-Cycle Fatigue Behavior of Tantalum (CR−1930)* (Washington: NASA)

Lempart M, Blad B, Adrian G, Bäck S, Knöös T, Ceberg C and Petersson K 2019 Modifying a clinical linear accelerator for delivery of ultra-high dose rate irradiation *Radiother. Oncol.* **139** 40–5

Loo B W, Schuler E, Lartey F M, Rafat M, King G J, Trovati S, Koong A C and Maxim P G 2017 (P003) Delivery of ultra-rapid flash radiation therapy and demonstration of normal tissue sparing after abdominal irradiation of mice *Int. J. Radiat. Oncol.* **98** E16

Marquardt E D, Le J P and Radebaugh R 2002 Cryogenic material properties database *11th International Cryocooler Conference* 681–7

Maxim P G, Tantawi S G and Loo B W 2019 PHASER: A platform for clinical translation of FLASH cancer radiotherapy *Radiother. Oncol.* **139** 28–33

Miller R B 2005 *Electronic Irradiation of Foods: An Introduction to the Technology* (New York, NY: Springer)

Montay-Gruel P *et al* 2017 Irradiation in a flash: Unique sparing of memory in mice after whole brain irradiation with dose rates above 100 Gy/s *Radiother. Oncol.* **124** 365–9

Montay-Gruel P *et al* 2018 X-rays can trigger the FLASH effect: Ultra-high dose-rate synchrotron light source prevents normal brain injury after whole brain irradiation in mice *Radiother. Oncol.* **129** 582–8

Montay-Gruel P *et al* 2021 Hypofractionated FLASH-RT as an effective treatment against glioblastoma that reduces neurocognitive side effects in mice *Clin. Cancer Res.* **27** 775–84

Naseri A and Mesbahi A 2010 A review on photoneutrons characteristics in radiation therapy with high-energy photon beams *Rep. Pract. Oncol. Radiother.* **15** 138–44

Nelson C 2020 Material Properties of Tantalum Including High Cycle Fatigue *JPS Conf. Proc.* **28** 081005

Ophoven N, Mauerhofer E, Li J, Rücker U, Zakalek P, Baggemann J, Gutberlet T, Brückel T and Langer C 2021 Monte Carlo simulation of proton- and neutron-induced radiation damage in a tantalum target irradiated by 70 MeV protons *Appl. Phys. A* **127** 1–14

Pan Z 2012 *Comparative Study of The Effect of Impurities on the Ductility Of Tantalum and Tungsten Based on Atomistic And First Principles Calculations* The University of North Carolina, Charlotte Phd Thesis

Papakyriacou M, Mayer H, Plenk H and Stanzl-Tschegg S 2002 Cyclic plastic deformation of tantalum and niobium at very high numbers of cycles *Mater. Sci. Eng. A* **325** 520–4
Papakyriacou M, Mayer H, Pypen C, Plenk H and Stanzl-Tschegg S 2001 Influence of loading frequency on high cycle fatique properties of b. c.c and h.c.p. metals *Mater. Sci. Eng. A* **308** 143–52
Rogers D W O, Walters B and Kawrakow I 2017 *BEAMnrc users manual Report No. PIRS-0 509(A), rev. L*
Rudd P J, Prior D and Austin-Smith S 2007 Neutron contamination of 10 MV X-rays: its relevance to treatment room door and maze design *Br. J. Radiol.* **80** 469–75
Schardt P, Deuringer J, Freudenberger J, Hell E, Knüpfer W, Mattern D and Schild M 2004 New x-ray tube performance in computed tomography by introducing the rotating envelope tube technology *Med. Phys.* **31** 2699–706
Schmidt F F and Ogden H R 1963 *The Engineering Properties of Tantalum and Tantalum Alloys (DMIC Report 189)* (Columbus: OH: DMIC)
Schulz K C and Yahr G T 1995 *Preliminary Fracture Analysis of the Core Pressure Boundary Tube for the Advanced Neutron Source Research Reactor (ORNL/M-4619)* (Oak Ridge, TN: ORNL)
Shelbaya O, Angus T, Baartman R, Jung P M, Kester O, Kiy S, Planche T and Rädel S D 2021 Autofocusing drift tube linac envelopes *Phys. Rev. Accel. Beams* **24** 124602
Simmons D A *et al* 2019 Reduced cognitive deficits after FLASH irradiation of whole mouse brain are associated with less hippocampal dendritic spine loss and neuroinflammation *Radiother. Oncol.* **139** 4–10
Van Marlen P, Dahele M, Folkerts M, Abel E, Slotman B J and Verbakel W F A R 2020 Bringing FLASH to the clinic: treatment planning considerations for ultrahigh dose-rate proton beams *Int. J. Radiat. Oncol. Biol. Phys.* **106** 621–9
Vozenin M C *et al* 2018 The Advantage of FLASH Radiotherapy Confirmed in Mini-pig and Cat-cancer Patients *Clin. Cancer Res.* **25** 35–42
Vozenin M C, Hendry J H and Limoli C L 2019 Biological benefits of ultra-high dose rate flash radiotherapy: sleeping beauty awoken *Clin. Oncol.* **31** 407–15
Walters B, Kawrakow I and Rogers D W O 2017 *DOSXYZnrc Users Manual Report No. PIRS-794, rev. B* (Ottawa: NRC: Ionizing Radiation Standards at the National Research Council of Canada)
Wilcox D 2016 Simulating performance of tantalum-clad tungsten targets *IWSMT* **13**
Wilcox D, Loveridge P, Davenne T, Jones L and Jenkins D 2018 Stress levels and failure modes of tantalum-clad tungsten targets at ISIS *J. Nucl. Mater.* **506** 76–82
Yahr G T 1993 *Fatigue Design Curves for 6061-T6 Aluminum* (Oak Ridge: TN: ORNL)